Infraslow locus coeruleus activity coordinates spindle rhythms and heart rate to gate fluctuating non-REM sleep substates

Alejandro Osorio-Forero, Romain Cardis, Gil Vantomme[1], Aurélie Guillaume-Gentil, Georgia Katsioudi[2], Laura M.J. Fernandez, Anita Lüthi[3]

Affiliation: Department of Fundamental Neurosciences, University of Lausanne, Rue du Bugnon 9, CH-1005 Lausanne, Switzerland

1 Present address: Department of Neurology, Wu Tsai Neurosciences Institute, Stanford University, 290 Jane Stanford Way, Stanford, CA94305, USA

2 Present address: Center for Integrative Genomics, University of Lausanne, Génopode, 1015 Lausanne, Switzerland

3 Corresponding author, e-mail: anita.luthi@unil.ch

Article Information:

Number of pages: 52

Total number of words (Introduction, Results, Discussion): 4,745

Number of Figures: 7

Number of words in Abstract: 150

Number of Supplementary Figures: 5

Number of references: 58 (+4 for Methods)

Keywords: continuity-fragility, arousability, parasympathetic, heart rate variability, targetted memory reactivation, hyperpolarization-activated cation channels

The continuity of non-rapid-eye-movement sleep (NREMS) is essential for its functions. However, many mammalian species, including humans, show NREMS fragility to maintain environmental vigilance. The neural substrates balancing NREMS continuity and fragility substates are unexplored. We show that the locus coeruleus (LC) is necessary and sufficient to generate infraslow (~50 s) continuity-fragility fluctuations in mouse NREMS. Through machine-learning-guided closed-loop optogenetic LC interrogation, we suppressed, locked, or entrained continuity-fragility fluctuations, as evident by LC-mediated regulation of sleep spindle clustering and heart rate variability. Noradrenergic modulation of thalamic but not cortical circuits was required for infraslow sleep spindle clustering and involved rapid noradrenaline increases that activated both α1- and β-adrenergic receptors to cause slowly decaying membrane depolarizations. The LC thus coordinates brain and bodily states during NREMS to engender continuity-fragility, accentuating its role in the physiology of sleep-related sensory uncoupling and as target in sleep disorders showing abnormal cortical and/or autonomic arousability.

Introduction

During sleep, behavioral interaction with the sensory environment is suppressed. The reduced response to external stimuli ensures a continuity of sleep in time that is necessary for its restorative and beneficial effects[1]. However, across the vertebrate kingdom, many species show adaptive mechanisms to continue monitoring their sensory environment while asleep. For example, unihemispheric sleep permits dolphins to continue surfacing to breathe or birds to engage in long-duration flights[2]. Sleeping humans also show sensory processing and cognitive elaboration of external stimuli during non-rapid-eye-movement sleep (NREMS) and REM sleep[3]. Incorporating sleep fragility to allow sensory vigilance could represent an adaptive strategy to trade-off between the benefits and risks of suppressed interactions with the environment. However, the neural implementations of such trade-off have not been pursued systematically. Therefore, it is unclear whether continuity-fragility dynamics are part of the design of vertebrate sleep-wake control circuits or reflect species-specific adaptations to particular ecological constraints.

Examinations of sensory arousability in rodent suggest that sensory isolation and environmental monitoring during NREMS occur, at least in part, sequentially in time. Based on monitoring arousability in response to auditory[4] or visual[5] stimuli, consolidated NREMS could be divided into substates of continuity and fragility that showed low and high arousability, respectively. Continuity-fragility substates alternated on an infraslow time scale of ~50 s (~0.02 Hz) and were accompanied by coordinated fluctuations in central and autonomic physiological correlates that were also found in human sleep[4]. These involved the electroencephalographic (EEG) spectral power component representing sleep spindles in the 10 – 15 Hz range, known to arise in thalamus and to be sleep-protective[3,6], and hippocampal ripples that are implied in sleep-dependent memory consolidation[7]. Moreover, both heart rate (HR) and pupil diameter co-varied such that increases coincided with low spindle occurrence. Infraslow variations are also prevalent in human NREMS, appearing in band-limited and full-band power EEG recordings, intracranial recordings, and in functional resonance imaging signals[4,8]. The time scale is also prominent in human cyclic alternating patterns, referred to as unstable sleep[9], in epilepsy and in abnormal arousal events in sleep-related movement and breathing disorders (reviewed in ref. [6]). However, the neural drives of infraslow

dynamics during NREMS have remained open, although neural and astrocytic mechanisms have been suggested[10].

Already the first recordings of action potentials in the sleeping animal indicated that wake-promoting brain areas retained some activity during NREMS[11-14]. The locus coeruleus (LC), the most dorsal of ten noradrenergic nuclei located in the pontine brain stem[11], ramifies widely within both the forebrain and the autonomic premotor nuclei[15] and coordinates neural and somatic conditions during wakefulness[16]. The LC discharges irregularly but continuously at 1 – 5 Hz when awake[11], but phasic discharges around 10 – 15 Hz precede autonomic and behavioral adaptations to unexpected stimuli in animals[17] and probably also in humans[18]. LC activity during NREMS coincides with the appearance of EEG or hippocampal sleep spindles[11,19,20] or cortical slow waves[21,22]. Opto- or chemogenetic LC stimulation in NREMS of rodents lowers auditory arousal thresholds[23] and increases resting state connectivity in salience networks[24], which is a signature of enhanced vigilance. Variations of LC activity during NREMS could thus be relevant for continuity-fragility fluctuations. Here, we used closed-loop real-time optogenetic modulation of LC activity in combination with global and local sleep recordings, HR monitoring, fiber photometric assessment of norepinephrine (NE) levels and the analysis of synaptic potentials generated by LC afferents in vitro. We demonstrate that infraslow activity variations in LC occur in natural undisturbed NREMS and coordinate central and autonomic physiological correlates underlying continuity-fragility fluctuations of NREMS.

Results

Noradrenergic signaling in thalamus is crucial for the clustering of sleep spindles during NREMS

Freely behaving mice sleep in NREM-REM sleep bouts interspersed by wakefulness during the light period (ZT0-12), which is their preferred resting phase. Figure 1a presents the sleep-wake behavior of a single mouse showing a hypnogram obtained from polysomnographic recordings between ZT1 and ZT9 and the corresponding time-frequency distribution derived from local field potential (LFP) recordings in the primary somatosensory cortex S1 (see Methods). From this distribution, power dynamics in two frequency bands characteristic for NREMS, the sigma (10 – 15 Hz) and the delta (1.5 – 4 Hz) frequency bands, were calculated. As shown previously[4], prominent power fluctuations in the sigma but not the delta

frequency band (10 – 15 Hz) determine NREMS continuity-fragility substates on an infraslow time interval with a peak around ~0.02 Hz (~50 s) (Fig. 1b). The sigma frequency band is populated by sleep spindles[6] that contribute to sensory decoupling during NREMS[3,6]. To determine whether sleep spindle density co-varied over 0.02 Hz, we used a previously developed sleep spindle detection algorithm[25] (Extended Data Fig. 1) and analyzed the phase-locking between sigma power and sleep spindle density in n = 33 mice (12 C57BL/6J and 21 dopamine-beta-hydroxylase (DBH)-Cre mice) recorded during the light phase. Sleep spindles clustered at the peak of the 0.02 Hz-fluctuation in sigma power, whereas they were rare in the troughs (Fig. 1c,d). Polar plots depicting the phase coupling of 168,097 spindles of 33 mice to the 0.02 Hz-fluctuation demonstrate the non-uniformity of this distribution (Fig. 1d; R of Rayleigh 0.51 ± 0.07; $P < 1.0*10^{-16}$). Sleep spindles thus cluster on the 50-s time scale during NREMS, in line with the infraslow fluctuation of sigma power and consistent with reports in mice and human[26,27].

To elucidate the role of noradrenergic signaling for infraslow variations in spindle density, we pharmacologically blocked noradrenergic receptors in thalamus, within which sleep spindles originate[6]. C57BL/6J mice implanted for polysomnography and S1 LFP recordings were injected with a mix of α1- and β- noradrenergic antagonists (0.1 mM Prazosine hydrochloride and 5 mM ((S)-(-)-atenolol, 150 nl, n = 6) or control artificial cerebrospinal fluid (ACSF, 150 nl, n = 6) locally into the somatosensory thalamus (see Methods). Noradrenergic antagonist but not ACSF injections resulted in a rapid and reversible reduction of the strength of the 0.02-Hz fluctuation in sigma power (Fig. 1e,f; Extended Data Fig. 2; P = 0.031). Moreover, instead of being clustered, sleep spindles now appeared irregularly and at a mean density that was ~2-fold higher (Fig. 1f; $P = 3.9*10^{-4}$). The properties of individual spindle events including amplitude, intra-spindle frequency, number of cycles and duration, showed minor changes (Extended Data Fig. 3). Noradrenergic signaling appears thus necessary for the generation of spindle-free periods resulting in their repeated clustering on the infraslow time scale.

Activity of the locus coeruleus is necessary and sufficient for the infraslow clustering of sleep spindles

To optogenetically interfere with the activity of the noradrenergic LC during NREMS in a time-controlled manner, we virally infected LC neurons of DBH-Cre mice to express excitatory (hChR2(H134R)

(ChR2); n = 11) or inhibitory (Jaws; n = 10) opsins. We then implanted these animals with EEG/EMG, an S1 LFP electrode and an optic fiber positioned uni- (for ChR2-injected animals) or bilaterally (for Jaws-injected animals) over the LC (Fig. 2a,b). Optimal fiber positioning was ensured through intra-surgical pupil diameter monitoring (Extended Data Fig 4). Using closed-loop monitoring of vigilance states, we first stimulated the LC specifically during NREMS at a low frequency (1 Hz) (Fig. 2c), and confirmed the successful expression of the opsins post mortem (Fig. 2d). The 1-Hz frequency is within the range of spontaneous LC unit activity during NREMS[19,21,28] and does not cause arousal when used to stimulate the LC optogenetically[19,29]. Stimulation sessions took place in the first 20 min of each hour during 8 h of the light phase (ZT1-9), with light or sham (during which the light source was turned off) stimulation alternating over successive recording days. Light stimulation in NREMS produced a rapid onset and almost complete suppression of sigma power and of sleep spindles. The effect lasted as long as light was present and instantly recovered once optogenetic stimulation stopped (Fig. 2e), decreasing the strength of the 0.02 Hz-fluctuation and sleep spindle density (Fig. 2f; n = 11, $P = 1.5*10^{-6}$ for the strength of the 0.02-Hz fluctuation, $P = 5.2*10^{-7}$ for spindle density). Conversely, continuous optogenetic inhibition according to the same experimental protocol locked sigma power at high levels and prolonged phases of high spindle occurrence (Fig. 2g,h; n = 10, $P = 2.0*10^{-3}$ for the strength of the 0.02-Hz fluctuation, $P = 2.0*10^{-3}$ for spindle density). These results demonstrate that LC activity is both necessary and sufficient for the 0.02 Hz-fluctuation and the clustering of sleep spindles.

To ensure that the LC interrogation did not disrupt NREMS, we quantified total times spent in the different vigilance states. We found that LC stimulation prolonged total time spent in NREMS at the expense of REM sleep and wakefulness (Fig. 2i), whereas LC inhibition had mild but opposite effects (Fig. 2j). These architectural alterations were not accompanied by significant changes in relative delta power (stimulation: increase by 13%, p = 0.10; inhibition: decrease <1%, p = 0.9). Therefore, low-frequency LC activity appears to consolidate NREMS without concomitant major changes in low-frequency spectral activity. This could be explained by the incompatibility of monoaminergic signaling with REM sleep, which would cause NREMS to continue[11,20,30].

Locus coeruleus fiber activation in thalamus but not in the cortex is relevant for sleep spindle clustering

From their thalamic site of origin, sleep spindle activity propagates to cortical circuits[6]. As LC innervates both thalamic and cortical brain areas[31], we tested the involvement of both innervation sites in the effects observed by direct LC stimulation. We placed the optic fiber over somatosensory thalamus or S1. For S1, the optic fiber stub was glued to the S1 LFP electrode at a distance of 800 – 1,200 µm over the tip. Light stimulation of thalamic LC afferents reproduced the suppressive effects observed with direct LC stimulation (Fig. 3 a,b; n = 6, $P = 5.6*10^{-4}$ for the strength of the 0.02-Hz fluctuation; $P = 0.014$ for spindle density). In contrast, cortical stimulation was ineffective (Fig. 3 c,d; n= 5, $P = 0.44$ for the strength of the 0.02-Hz fluctuation; $P = 0.63$ for spindle density). Thus, synaptic noradrenergic activity within the thalamus appears to sensitively control the clustering of sleep spindles measured in S1, in agreement with the pharmacological results in Fig 1.

Locus coeruleus activity fluctuates between high and low levels on an infraslow time scale

LC cells can discharge action potentials in both tonic and phasic modes during wakefulness, and both these modes have also been proposed to occur during NREMS[11,20,21]. To address whether time variations in LC activity were relevant for infraslow clustering of sleep spindles, we restricted the optogenetic manipulation of LC activity to distinct phases of the infraslow cycles. We detected these phases online through a machine-learning algorithm and triggered optogenetic activation based on whether sigma power started to rise or decline, thereby targetting large portions of fragility or continuity periods[32] (Fig. 4). When we optogenetically activated LC whenever sigma power started rising, the 0.02-Hz fluctuation was suppressed (Fig. 4 a,b; n = 9, $P = 4.4*10^{-9}$ for the strength of the 0.02-Hz fluctuation, $P = 2.2*10^{-6}$ for spindle density). This indicates that sigma increases, and sleep spindle generation, are not compatible with high LC activity. Conversely, when we inhibited LC when sigma power started declining, sigma power fluctuations became disrupted and tended to persist at high levels, thereby increasing sleep spindle density (Fig. 4 c,d; n = 10, $P = 2.0*10^{-3}$ for the strength of the 0.02-Hz fluctuation, $P = 5.9*10^{-3}$ for spindle density). The decline in sigma power thus required LC activity. These two results are best

compatible with LC activity showing an infraslow variation that is opposite to the one of the sigma power and sleep spindles, being high during the fragility periods and low during continuity periods, respectively.

Based on this result, we predicted that the converse experiment, stimulating LC during fragility or inhibiting it during continuity, would not disrupt infraslow dynamics. Intriguingly, when LC was activated while sigma power was declining, successive cycles of high sigma power kept appearing (Fig. 4e). Close inspection revealed that cycles appeared at shorter time intervals (sham: 52.9 ± 0.7 s, stim: 44.6 ± 1.7 s, n = 9, $P = 5.0*10^{-7}$, paired *t*-test) and were more regular, as evident by the decreased peak-to-peak variability (Fig. 4f; n = 9, $P = 5.2*10^{-5}$). Strengthening LC activity during fragility periods thus entrained a regular and faster infraslow fluctuation. When we specifically inhibited LC activity during online detected continuity periods, an entrainment was again observed, with interpeak intervals shortened (Fig. 4g; sham: 53.7 ± 2.6, inhibition: 50.8 ± 1.5 s, n = 9, $P = 3.6*10^{-3}$, paired *t*-test) and regularized (Fig. 4h; n = 10, $P = 0.049$). This indicates that a low level of LC activity remained during continuity periods that was inhibited by the light, thereby enforcing LC silency during sigma build-up and regularizing spindle appearance. Together, these results bring about a functionally relevant LC activity pattern during NREMS that interchanges between high, perhaps more phasic, and low, probably tonic, activity at infraslow timescales.

Rapid increases of noradrenaline levels in the thalamus precede the suppression of sleep spindles

High LC activity is expected to release NE within thalamus and to stimulate noradrenergic receptors as long as NE uptake is not completed. However, it is unclear how the time course of free NE and receptor signaling determine the time course of sleep spindle dis- and re-appearance. We used fiber photometry to measure free NE levels in thalamic nuclei across the sleep-wake cycle by expressing the newly developed fluorescent NE biosensor $GRAB_{NE1h}$[33] (see Methods). Mice expressing the NE biosensor in thalamus were implanted for sleep monitoring and fiber photometry. The fluorescence signals varied characteristically across the three vigilance states, including a pronounced decline during REM sleep, reminiscent of observations in prefrontal cortex (Fig. 5a)[20]. Focusing on NREMS bouts only, NE signals were inversely correlated with sigma power and showed recurrent negative peaks at infraslow intervals

(Fig. 5b). To resolve the time course of noradrenergic signaling on a cycle-to-cycle basis, we detected all infraslow sigma power cycles taking place during NREMS (excluding transitional periods) and examined the corresponding dynamics of free NE (Fig. 5c). Major increases in NE levels were detected before sigma power declined, consistent with the suppressant effects of LC activity. In contrast, NE levels were comparatively low as sigma power was rising at the beginning of the cycle. Therefore, NE increases suppress sigma power while NE decays seemed not tightly linked to the sigma power increases.

Ionic mechanisms underlying norepinephrine-induced infraslow membrane depolarizations

The effects of NE on neuronal excitability determine thalamic engagement in spindle-like rhythms[34], but the time range and actions of NE released by LC fibers on thalamic membrane potential and excitability are unknown. We hence combined patch-clamp recordings with optogenetic LC fiber stimulation to quantify cellular noradrenergic responses. We studied thalamocortical and thalamic reticular neurons, both of which are involved in sleep spindle generation[6]. From DBH-Cre mice expressing ChR2 in LC, we prepared coronal thalamic slices and recorded from cells in the ventrobasal complex, which contains the somatosensory thalamus. Thalamocortical cells had resting membrane potentials between -65 to -70 mV, and responded with rebound burst discharge upon negative current injection (Extended Data Fig. 5). Optogenetic stimulation generated a slow membrane depolarization for stimulation frequencies at 1, 3 and 10 Hz (Fig. 6a). Amplitudes of evoked potentials ranged between 0.8 – 4.5 mV with onset latencies of 1.25 – 6.9 s, and decayed with a slow time course lasting 66 – 106 s (Fig. 6b, Extended Data Fig. 5; n = 6 – 8). Only onset latency was modulated by stimulation frequency. The optogenetically evoked noradrenergic currents measured in cells voltage-clamped at -70 mV were blocked by atenolol (10 μM in bath, n = 5, $P = 0.049$), indicating involvement of β-adrenergic receptors (Fig. 6c,d)[34]. Furthermore, the current response was largely eliminated by bath application of 1.5 – 3 mM Cs^+ (Fig. 6e,f; n = 6, $P = 5.4 \times 10^{-4}$), a blocker of cAMP-sensitive hyperpolarization-activated cation-channels[35]. Both atenolol and Cs^+ produced outward currents, indicating a standing receptor and current activation.

To estimate the time course of action of NE on spindle-related cellular activity, we combined optogenetic stimulation of LC fibers with negative current injections to generate repetitive low-threshold

burst discharges[35], known to occur during sleep spindles (Fig. 6g)[6]. This resulted in a persistent afterdepolarization that was larger and longer than the one generated by cellular bursting alone (Fig. 6h; n = 7, P = 0.043). The coincidence of sleep spindle activity with NE release thus generates a prolonged period of cellular depolarization, known to be sufficient to render thalamocortical cells refractory to synaptically-driven burst discharge, which is necessary to engage in a next sleep spindle[35].

Light-induced depolarizations were also observed in thalamic reticular cells recorded in the somatosensory sector of TRN (Fig. 6i,j). Corresponding currents were largely blocked by the α1-adrenergic antagonist prazosin (5 μM in bath) (Fig. 6k,l; n = 3; P = 0.014)[34]. However, < 15% of TRN cells showed a detectable current response (Fig. 6m), suggesting a functional heterogeneity of these cells with respect to noradrenergic modulation[36]. Thalamic reticular cells thus also respond with slowly decaying membrane depolarizations when exposed to NE release from LC fibers.

The locus coeruleus coordinates heart rate variability with sigma power on the infraslow time scale through parasympathetic signaling

As NREMS fluctuates between continuity and fragility, sigma power is anticorrelated with the HR on an infraslow time scale[4]. Is the LC involved in this coordination? Through conjointly monitoring HR and sigma power in freely sleeping C57BL/6J mice (Fig. 7a,b), we found that HR variations were suppressed by the peripheral parasympathetic antagonist methylatropine (10 mg kg^{-1}) (Fig. 7c,d; n = 7, P = 0.035) but not by the peripheral sympathetic antagonist atenolol (1 mg kg^{-1}) (Fig. 7e,f; n = 12, P = 0.74) (see Methods).

LC activity has been implied in parasympathetically driven HR variability in humans[37] and, in rodents, augments inhibitory input to preganglionic cardiac vagal neurons[38]. Therefore, we next tested whether optogenetic manipulation of LC affected variations in HR. Indeed, continuous LC stimulation during NREMS disrupted the infraslow HR variations (Fig. 7g) and decreased its anticorrelation with sigma power (Fig. 7h; n = 10, $P = 4.1 \times 10^{-3}$). To directly evaluate the capability of LC in entraining HR variations as we observed for sigma power (see Fig. 4e), we stimulated LC specifically during fragility periods. This visibly augmented HR variations and generated anticorrelations with side-peaks showing an infraslow periodicity (Fig. 7i,j; n = 8). These data show that the LC is a source of HR variability during

NREMS on an infraslow timescale. Moreover, LC is capable of coordinating sigma power and HR in a manner that supports a critical role in the generation of NREMS continuity and fragility substates.

Discussion

Noradrenergic cell groups in the rostral hindbrain are conserved across mammals, reptiles, amphibians, birds and fish[39], and they are central for wakefulness and vigilance towards the sensory world[17]. Here, we establish an analogous function for the mammalian LC during NREMS. Through imposing fluctuations in brain and body correlates of sensory arousability, the LC drives NREMS between two opposite states of continuity and fragility. Mechanistically, these are distinct by infraslow membrane fluctuations ot thalamic networks and by different HR, caused by NE-induced activation of α1- and β-adrenergic receptors and by regulation of autonomic parasympathetic output, respectively.

The infraslow time scale has not only been found in mammalian NREMS[8], but it also appears as a time scale over which reptile sleep switches between two electrophysiologically distinct sleep states[40]. This raises the possibility that infraslow time intervals are a phylogenetically preserved temporal unit to maintain vigilance that arises from fluctuating noradrenergic input during NREMS. This possibility could spur future comparative studies on the phylogeny of sleep states and how these relate to species-specific noradrenergic activity during sleep[2]. Furthermore, the human noradrenergic system remains active during NREMS[22], during which it is critical for memory consolidation[41], expression of plasticity-related genes[42] and perhaps for dreams[43]. As sleep spindles serve as EEG hallmarks to distinguish light and deep sleep states in human[6], monitoring the LC in human sleep could also shed light on these and other[9,44] unique aspects of primate sleep. Finally, there is strong evidence that LC and sleep disruptions could be linked in post-traumatic stress disorders[45], in neurodegenerative diseases such as Alzheimer's and Parkinson's disease[44,46] and in insomnia[47]. Our findings highlight a need to further develop tools to monitor LC activity in human sleep as a possible neural target for the origin of these sleep disruptions. Furthermore, we suggest that looking at the detailed temporal organization of sleep spindle occurrence[48] could help to gain insight into noradrenergic activity in human NREMS.

Implications of infraslow LC activity variations for NREMS heterogeneity and targetted memory reactivation

We find that the major wake-promoting noradrenergic nucleus of the mammalian brain is functionally active during NREMS, elevating NE levels in a pulsatile manner within thalamus. Similar patterns of free NE were also found in prefrontal cortex[20], suggesting that there is a fluctuating neuromodulatory tone of NE throughout the forebrain during NREMS. We directly show that these pulses affect primary thalamic sensory neuron excitability, underscoring previous propositions of NREMS as a heterogeneous state with distinct levels of sensory arousability[4,5]. Future research will examine whether the brain states accompanied by variable LC activity differ with respect to other neuromodulators and electrical activity patterns, as proposed for hippocampal ripples[4] or cortical slow waves[22,28,43]. Of particular interest will also be to determine whether variations in functional connectivity during NREMS[49], area-specific spectral properties[25] and cortical dendritic Ca^{2+} activity[50], other polysomnographic measures of unstable sleep[9] or other forms of behavioral output[51] relate to LC. Intriguingly, a recent study pointed out that the optimal timing of targetted memory reactivation via auditory stimuli depends on sleep spindle variations that involve infraslow timing[48]. This reinforces the notion that NREMS is segregated into functionally distinct states that also concern the sleeping brain's capability of neuronal ensemble reactivation and the replay of memory traces, which are prerequisites for memory consolidation[7].

LC-dependent control of sensory arousability during NREMS

LC activity likely controls sensory arousability through several mechanisms. First, LC responds to sensory stimuli[14], therefore, if LC neurons depolarize and discharge more action potentials, sensory throughput will be enhanced[23]. Second, LC-mediated sleep spindle suppression removes inhibitory constraints on the successful propagation of sensory inputs across the thalamocortical axis[6]. Third, sensory-evoked discharge of single or multiple thalamic and cortical units is strengthened by LC stimulation, with thalamic neurons increasing sensory responsiveness more robustly[52]. The density of LC fiber varicosities is higher in rat somatosensory thalamic compared to cortical areas[31]. In both rodents and humans, noradrenergic signaling strengthens precisely those resting state networks that optimize vigilance and perception in response to pending important input[24,53]. These findings offer several entry

points to further examine how noradrenergic modulation of thalamic circuits facilitates the processing of sensory stimuli during states of NREMS.

The role of LC for sleep spindles

Evidence that LC activity suppresses spindle activity is available for electrographically detected sleep spindles measured in hippocampus[19] and for spindles in bipolar EEG derivations[20]. Furthermore, NE levels in prefrontal cortex are low when the EEG shows spindles[20]. We demonstrate a direct mechanistic opposition between NE levels and the circuits in which sleep spindles originate. First, we rapidly and reversibly suppress local sleep spindles[25] via optogenetic LC activation and second, we find that free NE levels run opposite to locally generated sleep spindles. Third, we demonstrate that LC fiber activation promotes thalamic circuit refractoriness. The suppressive action of noradrenergic activity on sleep spindles has led to the proposition that LC activity will acutely terminate individual sleep spindle events[11,19]. However, we could not observe strong changes in sleep spindle properties in favor of this suggestion, when we pharmacologically antagonized noradrenergic signaling specifically in thalamus, although we previously identified our detection algorithm to sensitively detect regionally specific or genetically induced variations in sleep spindle properties[25]. Furthermore, we find that synaptic events caused by NE release rise slowly over seconds and are thus unlikely to shortcut individual spindle-events. Noradrenergic signaling seems instead tailored to generate prolonged relatively spindle-free periods as thalamic cells are brought into a depolarized state[35].

The cellular and ionic mechanisms underlying infraslow dynamics of sleep spindle clustering

The precise cellular mechanisms that underlie the particularly slow timing of the fluctuations in sigma power and spindle density have remained open[10]. We managed to dissect the temporal relationships between free NE levels and their ionic effects on thalamic spindle-generating circuits. The fiber photometric in combination with the cellular recording suggest that the ionic consequences of NE outlast the availability of free NE and are of primary interest as temporal determinants of the infraslow time scale. NE induces a slowly decaying membrane depolarization through activation of both α1- or β-receptors in thalamocortical and thalamic reticular neurons, which retards the re-engagement of these

cells in sleep spindle generation long after free NE levels have returned to baseline. In further support of this interpretation, we could entrain the infraslow fluctuations when we reinforced or attenuated LC activity at appropriate moments. The reinforcement of LC activity most likely triggered membrane depolarizations more consequentially across large cell populations, whereas the attenuation removed spurious LC activity, overall promoting a more synchronous entry and exit of thalamic circuits within the infraslow cycles. We remark that such a scenario does not preclude that other mechanisms causing individual spindles to terminate take place (reviewed in ref. [6]). Moreover, we currently cannot exclude that there are feedback mechanisms on the LC that modify, and perhaps accelerate, its endogenous infraslow activity.

To the best of our knowledge, the slow LC-triggered membrane depolarizations described here are the sole exclusively noradrenergically mediated postsynaptic effects described so far. LC fibers release glutamate to generate fast glutamatergic currents in parabrachial nucleus[54], with the release of NE remaining minor unless light pulses were applied repetitively at higher frequencies. We found instead that thalamic LC-fiber-elicited responses were relatively uniform in amplitude and time course over the 1 – 10 Hz frequency range. This could ensure a homogeneity of action on thalamic membrane potentials, resulting in a global depolarization across many neurons. Ultrastructural studies indeed suggest that noradrenergic terminals in the rodent ventrobasal complex do not form well-defined synaptic contacts[55], suggesting that released NE may diffuse from the site of release into the extracellular medium. Supporting this, we find that noradrenergic receptors activated by optogenetic LC fiber stimulation are the same as the ones targeted by bath-applied NE[34]. There also was a measurable noradrenergic antagonist-sensitive holding current component in our slices, consistent with an ambient NE level generating a tonic noradrenergic signal.

The LC as a source of heart rate variability

Initial studies on the continuity-fragility organization of NREMS pointed out that an infraslow periodicity was also present in the HR[4] and in pupil diameter[5]. The fragility period, during which spindles are infrequent and arousals more likely, was accompanied by a higher HR and a larger pupil diameter. Using peripherally acting drugs, we identified the parasympathetic system as key for the infraslow variations in HR, as also observed for pupil diameter variations[5]. The LC increases HR through multiple

pathways[15], amongst which one involves an inhibition of the parasympathetic preganglionic vagal nuclei[38] that is thought to underlie HR variability in humans[37]. Our study is the first to directly probe the consequences of specific optogenetic LC stimulation on HR, which needs to be further explored regarding frequency dependence, mechanisms and variation with vigilance state. Continuous 1 Hz-stimulation during NREMS abolished infraslow HR variations, thus demonstrating that LC acts to coordinate the infraslow activity patterns in brain and heart. Intriguingly, when we stimulated LC during fragility periods known to entrain sigma power fluctuations, we also increased the fluctuations of the HR and strengthened anticorrelations on the infraslow time scale. We thus establish the LC as a coordinator of brain and bodily fluctuations during NREMS, which likely involve parasympathetic signaling. This suggests that the LC neurons projecting to thalamus coordinate their activity with the ones projecting to the cardiac premotor vagal neurons, pointing to precise intra-LC mechanisms that subserve this coordination process. Furthermore, the direct demonstration of LC's role in HR variability could renew interest in the relation between HR variability and sleep disorders[56]. Finally, the neural systems underlying this coordination could reach beyond LC, as it is now clear that infraslow neuronal activities are present also in dorsomedial medulla during NREMS[57].

We find that mammalian sleep harnesses on wake promotion to enable sensory vigilance. This insight requires a renewal of current models of sleep-wake control in which reciprocal and exclusive antagonism is so far prevalent[58]. We are now able to concretize questions into the origins of a large variety of primary and secondary sleep disorders, in which hyperarousals, autonomic arousals and movement-related arousals prominently feature[9,44,47,51].

References

1 Van Someren, E. J. *et al.* Disrupted sleep: from molecules to cognition. *J Neurosci* **35**, 13889-13895, doi:10.1523/JNEUROSCI.2592-15.2015 (2015).

2 Mascetti, G. G. Adaptation and survival: hypotheses about the neural mechanisms of unihemispheric sleep. *Laterality*, 1-23, doi:10.1080/1357650X.2020.1828446 (2020).

3 Andrillon, T. & Kouider, S. The vigilant sleeper: neural mechanisms of sensory (de)coupling during sleep. *Curr Opin Physiol* **15**, 47-59, doi:10.1016/j.cophys.2019.12.002 (2020).

4 Lecci, S. *et al.* Coordinated infra-slow neural and cardiac oscillations mark fragility and offline periods in mammalian sleep. *Sci. Adv.* **3**, e1602026, doi:10.1126/sciadv.1602026 (2017).

5 Yüzgeç, O., Prsa, M., Zimmermann, R. & Huber, D. Pupil size coupling to cortical states protects the stability of deep sleep via parasympathetic modulation. *Curr Biol* **28**, 392-400 e393, doi:10.1016/j.cub.2017.12.049 (2018).

6 Fernandez, L. M. J. & Lüthi, A. Sleep Spindles: Mechanisms and Functions. *Physiol Rev* **100**, 805-868, doi:10.1152/physrev.00042.2018 (2020).

7 Klinzing, J. G., Niethard, N. & Born, J. Mechanisms of systems memory consolidation during sleep. *Nat Neurosci* **22**, 1598-1610, doi:10.1038/s41593-019-0467-3 (2019).

8 Watson, B. O. Cognitive and physiologic impacts of the infraslow oscillation. *Front Syst Neurosci* **12**, 44, doi:10.3389/fnsys.2018.00044 (2018).

9 Parrino, L., Halasz, P., Tassinari, C. A. & Terzano, M. G. CAP, epilepsy and motor events during sleep: the unifying role of arousal. *Sleep Med Rev* **10**, 267-285, doi:10.1016/j.smrv.2005.12.004 (2006).

10 Hughes, S. W., Lörincz, M. L., Parri, H. R. & Crunelli, V. Infraslow (<0.1 Hz) oscillations in thalamic relay nuclei: basic mechanisms and significance to health and disease states. *Prog Brain Res* **193**, 145-162, doi:10.1016/B978-0-444-53839-0.00010-7 (2011).

11 Aston-Jones, G. & Bloom, F. E. Activity of norepinephrine-containing locus coeruleus neurons in behaving rats anticipates fluctuations in the sleep-waking cycle. *J Neurosci* **1**, 876-886, doi: 10.1523/JNEUROSCI.01-08-00876.1981 (1981).

12 el Mansari, M., Sakai, K. & Jouvet, M. Unitary characteristics of presumptive cholinergic tegmental neurons during the sleep-waking cycle in freely moving cats. *Exp Brain Res* **76**, 519-529, doi:10.1007/BF00248908. (1989).

13 Kayama, Y., Ohta, M. & Jodo, E. Firing of 'possibly' cholinergic neurons in the rat laterodorsal tegmental nucleus during sleep and wakefulness. *Brain Res* **569**, 210-220, doi:0006-8993(92)90632-J [pii] (1992).

14 Takahashi, K., Kayama, Y., Lin, J. S. & Sakai, K. Locus coeruleus neuronal activity during the sleep-waking cycle in mice. *Neuroscience* **169**, 1115-1126, doi:10.1016/j.neuroscience.2010.06.009 (2010).

15 Samuels, E. R. & Szabadi, E. Functional neuroanatomy of the noradrenergic locus coeruleus: its roles in the regulation of arousal and autonomic function part II: physiological and pharmacological manipulations and pathological alterations of locus coeruleus activity in humans. *Curr Neuropharmacol* **6**, 254-285, doi:10.2174/157015908785777193 (2008).

16 Poe, G. R. *et al.* Locus coeruleus: a new look at the blue spot. *Nat Rev Neurosci* **21**, 644-659, doi:10.1038/s41583-020-0360-9 (2020).

17 Sara, S. J. & Bouret, S. Orienting and reorienting: the locus coeruleus mediates cognition through arousal. *Neuron* **76**, 130-141, doi:10.1016/j.neuron.2012.09.011 (2012).

18 Murphy, P. R., Robertson, I. H., Balsters, J. H. & O'Connell, R. G. Pupillometry and P3 index the locus coeruleus-noradrenergic arousal function in humans. *Psychophysiology* **48**, 1532-1543, doi:10.1111/j.1469-8986.2011.01226.x (2011).

19 Swift, K. M. *et al.* Abnormal locus coeruleus sleep activity alters sleep signatures of memory consolidation and impairs place cell stability and spatial memory. *Curr Biol* **28**, 3599-3609 e3594, doi:10.1016/j.cub.2018.09.054 (2018).

20 Kjaerby, C. *et al.* Dynamic fluctuations of the locus coeruleus-norepinephrine system underlie sleep state transitions. *Biorxiv*, doi:10.1101/2020.09.01.274977. (2020).

21 Eschenko, O. & Sara, S. J. Learning-dependent, transient increase of activity in noradrenergic neurons of locus coeruleus during slow wave sleep in the rat: brain stem-cortex interplay for memory consolidation? *Cereb Cortex* **18**, 2596-2603, doi:10.1093/cercor/bhn020 (2008).

22 Dang-Vu, T. T. *et al.* Spontaneous neural activity during human slow wave sleep. *Proc Natl Acad Sci U S A* **105**, 15160-15165, doi:10.1073/pnas.0801819105 (2008).

23 Hayat, H. *et al.* Locus coeruleus norepinephrine activity mediates sensory-evoked awakenings from sleep. *Sci Adv* **6**, eaaz4232, doi:10.1126/sciadv.aaz4232 (2020).

24 Zerbi, V. *et al.* Rapid reconfiguration of the functional connectome after chemogenetic *locus coeruleus* activation. *Neuron* **103**, 702-718 e705, doi:10.1016/j.neuron.2019.05.034 (2019).

25 Fernandez, L. M. *et al.* Thalamic reticular control of local sleep in sensory cortex. *Elife* **7**, e39111, doi:10.7554/eLife.39111 (2018).

26 Lázár, Z. I., Dijk, D. J. & Lázár, A. S. Infraslow oscillations in human sleep spindle activity. *J Neurosci Methods* **316**, 22-34, doi:10.1016/j.jneumeth.2018.12.002 (2019).

27 Csernai, M. *et al.* Dynamics of sleep oscillations is coupled to brain temperature on multiple scales. *J Physiol* **597**, 4069-4086, doi:10.1113/JP277664 (2019).

28 Eschenko, O., Magri, C., Panzeri, S. & Sara, S. J. Noradrenergic neurons of the locus coeruleus are phase locked to cortical up-down states during sleep. *Cereb Cortex* **22**, 426-435, doi:10.1093/cercor/bhr121 (2012).

29 Carter, M. E. *et al.* Tuning arousal with optogenetic modulation of locus coeruleus neurons. *Nat Neurosci* **13**, 1526-1533, doi:10.1038/nn.2682 (2010).

30 Wyatt, R. J., Chase, T. N., Kupfer, D. J., Scott, J. & Snyder, F. Brain catecholamines and human sleep. *Nature* **233**, 63-65, doi:10.1038/233063a0 (1971).

31 Agster, K. L., Mejias-Aponte, C. A., Clark, B. D. & Waterhouse, B. D. Evidence for a regional specificity in the density and distribution of noradrenergic varicosities in rat cortex. *J Comp Neurol* **521**, 2195-2207, doi:10.1002/cne.23270 (2013).

32 Cardis, R. *et al.* Local cortical arousals and heightened (somato)sensory arousability during non-REM sleep of mice in chronic pain. *Biorxiv*, 2021.01.04.425347, doi:10.1101/2021.01.04.425347 (2021).

33 Feng, J. *et al.* A genetically encoded fluorescent sensor for rapid and specific *in vivo* detection of norepinephrine. *Neuron* **102**, 745-761 e748, doi:10.1016/j.neuron.2019.02.037 (2019).

34 Lee, K. H. & McCormick, D. A. Abolition of spindle oscillations by serotonin and norepinephrine in the ferret lateral geniculate and perigeniculate nuclei *in vitro*. *Neuron* **17**, 309-321, doi:10.1016/s0896-6273(00)80162-2 (1996).

35 Lüthi, A. & McCormick, D. A. Modulation of a pacemaker current through Ca^{2+}-induced stimulation of cAMP production. *Nat Neurosci* **2**, 634-641, doi:10.1038/10189 (1999).

36 Vantomme, G., Osorio-Forero, A., Lüthi, A. & Fernandez, L. M. J. Regulation of local sleep by the thalamic reticular nucleus. *Front Neurosci* **13**, 576, doi:10.3389/fnins.2019.00576 (2019).

37 Mather, M. *et al.* Higher locus coeruleus MRI contrast is associated with lower parasympathetic influence over heart rate variability. *Neuroimage* **150**, 329-335, doi:10.1016/j.neuroimage.2017.02.025 (2017).

38 Wang, X., Pinol, R. A., Byrne, P. & Mendelowitz, D. Optogenetic stimulation of locus ceruleus neurons augments inhibitory transmission to parasympathetic cardiac vagal neurons via activation of brainstem α1 and β1 receptors. *J Neurosci* **34**, 6182-6189, doi:10.1523/JNEUROSCI.5093-13.2014 (2014).

39 Smeets, W. J. & Gonzalez, A. Catecholamine systems in the brain of vertebrates: new perspectives through a comparative approach. *Brain Res Brain Res Rev* **33**, 308-379, doi:10.1016/s0165-0173(00)00034-5 (2000).

40 Libourel, P. A. *et al.* Partial homologies between sleep states in lizards, mammals, and birds suggest a complex evolution of sleep states in amniotes. *PLoS Biol* **16**, e2005982, doi:10.1371/journal.pbio.2005982 (2018).

41 Gais, S., Rasch, B., Dahmen, J. C., Sara, S. & Born, J. The memory function of noradrenergic activity in non-REM sleep. *J Cogn Neurosci* **23**, 2582-2592, doi:10.1162/jocn.2011.21622 (2011).

42 Cirelli, C. & Tononi, G. Differential expression of plasticity-related genes in waking and sleep and their regulation by the noradrenergic system. *J Neurosci* **20**, 9187-9194, doi:10.1523/JNEUROSCI.20-24-09187.2000. (2000).

43 Siclari, F., Bernardi, G., Cataldi, J. & Tononi, G. Dreaming in NREM sleep: a high-density EEG study of slow waves and spindles. *J Neurosci* **38**, 9175-9185, doi:10.1523/JNEUROSCI.0855-18.2018 (2018).

44 Doppler, C. E. J. *et al.* Microsleep disturbances are associated with noradrenergic dysfunction in Parkinson's disease. *Sleep*, in press, doi:10.1093/sleep/zsab040 (2021).

45 Reist, C. *et al.* Prazosin for treatment of post-traumatic stress disorder: a systematic review and meta-analysis. *CNS Spectr*, 1-7, doi:10.1017/S1092852920001121 (2020).

46 Galgani, A. *et al.* Locus coeruleus magnetic resonance imaging in neurological diseases. *Curr Neurol Neurosci Rep* **21**, 2, doi:10.1007/s11910-020-01087-7 (2020).

47 Van Someren, E. J. W. Brain mechanisms of insomnia: new perspectives on causes and consequences. *Physiol Rev*, in press, doi:10.1152/physrev.00046.2019 (2020).

48 Antony, J. W. *et al.* Sleep spindle refractoriness segregates periods of memory reactivation. *Curr Biol* **28**, 1736-1743, doi:10.1016/j.cub.2018.04.020 (2018).

49 Stevner, A. B. A. *et al.* Discovery of key whole-brain transitions and dynamics during human wakefulness and non-REM sleep. *Nat Commun* **10**, 1035, doi:10.1038/s41467-019-08934-3 (2019).

50 Seibt, J. *et al.* Cortical dendritic activity correlates with spindle-rich oscillations during sleep in rodents. *Nat Commun* **8**, 684, doi:10.1038/s41467-017-00735-w (2017).

51 Ferri, R., Koo, B. B., Picchietti, D. L. & Fulda, S. Periodic leg movements during sleep: phenotype, neurophysiology, and clinical significance. *Sleep Med* **31**, 29-38, doi:10.1016/j.sleep.2016.05.014 (2017).

52 Devilbiss, D. M. & Waterhouse, B. D. The effects of tonic locus ceruleus output on sensory-evoked responses of ventral posterior medial thalamic and barrel field cortical neurons in the awake rat. *J Neurosci* **24**, 10773-10785, doi:10.1523/JNEUROSCI.1573-04.2004 (2004).

53 Hermans, E. J. *et al.* Stress-related noradrenergic activity prompts large-scale neural network reconfiguration. *Science* **334**, 1151-1153, doi:10.1126/science.1209603 (2011).

54 Yang, B. *et al.* Locus coeruleus anchors a trisynaptic circuit controlling fear-induced suppression of feeding. *Neuron* **109**, 1-16, doi:10.1016/j.neuron.2020.12.023 (2021).

55 Nothias, F., Onteniente, B., Roudier, F. & Peschanksi, M. Immunocytochemical study of serotoninergic and noradrenergic innervation of the ventrobasal complex of the rat thalamus. *Neurosci Lett* **95**, 59-63, doi:10.1016/0304-3940(88)90632-5 (1988).

56 Silvani, A., Calandra-Buonaura, G., Benarroch, E. E., Dampney, R. A. L. & Cortelli, P. Bidirectional interactions between the baroreceptor reflex and arousal: an update. *Sleep Med* **16**, 210-216, doi: 10.1016/j.sleep.2014.10.011 (2015).

57 Stucynski, J. A., Schott, A. L., Baik, J., Chung, S. & Weber, F. Regulation of REM sleep by inhibitory neurons in the dorsomedial medulla. *Biorxiv* 2020.11.30.405530, doi:10.1101/2020.11.30.405530 (2021).

58 Saper, C. B. & Fuller, P. M. Wake-sleep circuitry: an overview. *Curr Opin Neurobiol* **44**, 186-192, doi:10.1016/j.conb.2017.03.021 (2017).

59 Vantomme, G. *et al.* A thalamic reticular circuit for head direction cell tuning and spatial navigation. *Cell Rep* **31**, 107747, doi:10.1016/j.celrep.2020.107747 (2020).

60 Smith, R. D., Grzelak, M. E. & Coffin, V. L. Methylatropine blocks the central effects of cholinergic antagonists. *Behav Pharmacol* **5**, 167-175, doi:10.1097/00008877-199404000-00008 (1994).

61 Neil-Dwyer, G., Bartlett, J., McAinsh, J. & Cruickshank, J. M. β-adrenoceptor blockers and the blood-brain barrier. *Br J Clin Pharmacol* **11**, 549-553, doi:10.1111/j.1365-2125.1981.tb01169.x (1981).

62 Berens, P. CircStat: A MATLAB toolbox for circular statistics. *J Stat Software* **31**, 1-21, doi:10.18637/jss.v031.i10 (2009).

Online Methods.

Animal husbandry and numbers used for experiments

Mice from the C57BL/6J line and from the B6.FVB(Cg)-Tg(Dbh-cre)KH212Gsat/Mmucd (MMRRC Stock#036778-UCD) line, referred to here as DBH-Cre line, were bred on a C57BL/6J background and housed in a humidity- and temperature-controlled animal house with a 12 h / 12 h light-dark cycle (lights on at 9 am). Food and water were available ad libitum throughout all the experimental procedures. For viral injections, 2- to 7-week-old mice of either sex were transferred to a P2 safety level housing room with identical conditions 1 d prior to injection. For in vivo experimentation, animals were transferred to the recording room 3 d after viral injection and left to recover for at least 1 week prior to the implantation surgery, after which they were singly housed in standard-sized cages. The grids on top of the cage were removed and replaced by 30 cm-high Plexiglass walls. Fresh food was regularly placed on the litter and the water bottle inserted through a hole in the cage wall. Objects (tissues, paper rolls, ping-pong balls) were given to play. For in vitro experimentation, animals were transferred 3 d after viral injection to a housing room with identical conditions and were used 3 – 6 weeks after injection. In total, 12 male C57BL/6J mice were used for intracranial pharmacological experiments, 19 male C57BL/6J mice for cardiac pharmacology experiments and 6 male C57BL/6J mice for the fiber photometry experiments.

From the DBH-Cre line, 21 (11 males and 10 females) heterozygous Cre +/- animals were used for optogenetic experiments, and 14 (2 males and 12 females) for in vitro experiments. All experiments were conducted in accordance with the Swiss National Institutional Guidelines on Animal Experimentation and were approved by the Swiss Cantonal Veterinary Office Committee for Animal Experimentation.

Surgical procedures for viral injections

Optogenetics in vivo and in vitro: Animals were anaesthetized with ketamine (83 mg kg^{-1})/xylazine (3.5 mg kg^{-1}), kept on a thermal blanket to maintain body temperature around 37 °C, and injected i.p. with carprofen (5 mg kg^{-1}) for analgesia. Mice were then head-fixed on a stereotactic frame equipped with a head adaptor for young animals (Stoelting 51925). The scalp was disinfected, injected with a mix of lidocaine (6 mg kg^{-1})/bupivacaine (2.5 mg kg^{-1}) for local anesthesia and opened with scissors exposing the desired region of the skull. For the injections, we used a thin glass pipette (5-000-1001-X, Drummond Scientific) pulled on a vertical puller (Narishige), initially filled with mineral oil, and backfilled with the virus-containing solution just prior to injection. Injections took place at an injection rate of 100 – 200 nl min^{-1}. For optogenetic stimulation experiments, 2 animals were injected with a ssAAV5/2-hEF1α-dlox-hChR2(H134R)_mCherry(rev)-dlox-WPRE-hGHp(A) (titer: $9.1x10^{12}$ vg / ml, 0.8 – 1 µL) virus bilaterally in a region close to the LC. The stereotaxic coordinates were (relative to Bregma, given in mm here and throughout the rest of the Online Methods): lateral (L) ±1.28; antero-posterior (AP) -5.45, depth (D) -3.65), as done previously[29]. The remaining 9 animals were injected bilaterally with the same virus (0.3 – 0.6 µL) directly into the LC (L ±1.05; AP -5.45; D -3.06). The two viral injections yielded comparable results and data were pooled. For optogenetic inhibition, all animals were injected bilaterally into the LC (0.2 – 0.35 µL) with either pAAV5-CAG-FLEX-rc[Jaws-KGC-GFP-ER2] ($7x10^{12}$ vg / ml; n = 2, Addgene), AAV8-hSyn-FLEX-Jaws-KGC-GFP-ER2 ($3.2x10^{12}$ vg / ml; n = 3, UNC Vector Core) or ssAAV-5/2-hSyn1-dlox-Jaws_KGC_EGFP_ERES(rev)-dlox-WPRE-bGHp(A)-SV40p(A) (titer: $6.4x10^{12}$ vg / ml; n = 5, VVF Zürich).

Fiber photometry: For the assessment of NE dynamics in the thalamus, an AAV virus (ssAAV9/2-hSyn1-GRAB_NE1h-WPRE-hGHp(A), titer: $7.2x10^{12}$ vg / ml, VVF Zürich) containing the plasmid encoding a NE sensor (pAAV-hSyn-GRAB_NE1h, Addgene Plasmid #123309)[33] was injected into the thalamus (500 nl; L

2.0; AP -1.6; D -3.0). After the injections, the incision was sutured, and the area disinfected. Animals were carefully monitored and returned to the home cage once awake and moving around. Recovery time after injections took place for a minimum of 1 week before the next surgeries. Paracetamol was given in the water for the 4 postoperative days at a concentration of 2 mg ml^{-1}.

Surgical procedures for sleep recordings combined with optogenetics or fiber photometry

For in vivo EEG/EMG combined with local field potential (LFP) recordings, electrode implantation was as previously described[4,25,32]. In short, animals were anesthetized with isoflurane (1.5 – 2.5 %) in a mixture of O_2 and N_2O. After analgesia (i.p. carprofen 5 mg kg^{-1}) and disinfection, animals were fixed in a Kopf stereotax and injected into the scalp with a mix of lidocaine (6 mg kg^{-1})/bupivacaine (2.5 mg kg^{-1}) and a piece of the scalp was removed after 3 – 5 min, the skull exposed and the bone scratched to improve adhesion of the head implant. Then, we drilled small craniotomies (0.3 – 0.5 mm) over left frontal and parietal bones and positioned two conventional gold-coated wire electrodes in contact with the dura mater for EEG recordings. On the contralateral (right) side, a high-impedance tungsten LFP microelectrode (10–12 MΩ, 75 µm shaft diameter, FHC) was implanted in the primary somatosensory cortex (L 3; AP -0.7; D -0.85). Additionally, as a neutral reference, a silver wire (Harvard Apparatus) was inserted into the occipital bone over the cerebellum and two gold pellets were inserted into the neck muscles for EMG recordings. All electrodes were fixed using Loctite Schnellkleber 401 glue and soldered to a multisite connector (Barrettes Connectors 1.27 mm, male connectors, Conrad).

For intracranial injection of noradrenergic antagonists, we additionally made a craniotomy over the thalamus (L 2; AP -1.60) and covered it with a silicone-based sealant (Kwik-Cast Silicone Sealant, WPI). Additionally, we glued and cemented a light-weight metal head-post (Bourgeois Mécanique SAS, Lyon, France) onto the midline skull to perform painless head-fixation during injection of noradrenergic antagonists.

For optogenetic experiments, DBH-Cre animals were implanted with custom-made optic fibers[59]. A multimode fiber (225 µm outer diameter, Thorlabs, BFL37-2000/FT200EMT) was inserted and glued (heat-curable epoxy, Precision Fiber Products, ET-353ND-16OZ) to a multimode ceramic zirconia ferrule (Precision Fiber Products, MM-FER2007C-2300). The penetrating end was cut at the desired length with

a carbide-tip fiber optic scribe (Precision Fiber Products, M1-46124). The outside end was then polished using fiber-polishing films (Thorlabs). For optogenetic stimulation of the LC cell bodies (n = 11 animals) a single 3-mm fiber stub was implanted directly over the LC (L 1.0; AP -5.4; D -2.3). Out of the 11 animals, 6 animals were also implanted with a 3 mm-optic fiber stub over the somatosensory thalamus (L 2.0; AP -1.7; D -2.5). For the 5 additional animals, we implanted a custom-made optrode in S1 built with a high-impedance fine tungsten LFP microelectrodes (10 – 12 MΩ, 75 µm shaft diameter, FHC) glued to the stub of a 2 mm-optic fiber at a distance of 800 – 1,200 µm. The optrode was then inserted into S1 (L 3.0; AP -0.7; D 0.8). For optogenetic inhibition of the LC bodies (n = 10), bilateral optic fibers were implanted at a 20° lateral angle targeting the LC (L ±1.84; AP -5.4; D -2.47). To establish the final coordinates of the optic fibers, pupil diameter changes were monitored in a subgroup of 5 animals while lowering the optic fiber and applying light stimuli (Extended Data Fig. 4; 10 – 30 pulses at 10 Hz). A custom-made software developed in Matlab was used for image acquisition (See in vivo data analysis).

For fiber photometry experiments, in addition to the recording electrodes, we implanted C57BL/6J animals (n = 6) with a premade 400 µm-thick optic fiber coupled to a cannula (MFC_400/430-0.66_3.5mm_ZF1 25(G)_FLT, Doris Lenses) over the dorsal and reticular thalamus (L 1.8; AP -1.7; D 2.5) at a rate of 1 mm min^{-1}.

Finally, a dental cement structure was built to fix the implant in place. After disinfection with iodine-based cream, animals were returned to their home cage and kept in careful monitoring. Animals were provided with paracetamol (2 mg mL^{-1}) in the drinking water for at least 4 days after the procedure.

In vivo electrophysiological recordings

Once recovered from the surgery, animals were habituated to the cabling for 5 – 7 days, followed by a baseline recording to ascertain the quality of the signals. We acquired the EEG, EMG and LFP signals at a 1 kHz sampling frequency using an Intan digital RHD2132 amplifier board and a RHD2000 USB Interface board (Intan Technologies) connected via SPI cables (RHD recording system, Intan Technologies). Homemade adapters containing an Omnetics - A79022-001 connector (Omnetics Connector Corp.) linked to a female Barrettes Connector (Conrad) were used as an intermediate between

the head implant of the animal and the headstage. We acquired the data with Matlab using the RHD2000 Matlab toolbox and a customized software in the same environment[25,32].

Experimental Procedures for intracranial local pharmacology

We gently and gradually habituated mice to being head-fixed by increasing the amount of time spent in head fixation daily from 5 min to 45 min over a period of 4 – 5 days. The rest of the time, the animals spent being tethered to the recording system in their home cage. On the first experimental day, we removed the silicone cover of the craniotomy in head-fixed conditions and positioned a glass pipette (5-000-1001-X, Drummond Scientific, pulled on a vertical Narishige PP-830 puller, tip size of 15 – 25 µm) over the craniotomy and waited for 30 min while gently touching the side of the craniotomy to simulate an injection. Then, we covered the craniotomy again with the silicone-based sealant and returned the animals to the home cage for an 8 h-baseline polysomnographic recording. The next day, we removed the silicone again and injected 150 nL of noradrenergic antagonists or ACSF at two different depths within the thalamus (D: -3.2 and -2.8 mm). For the experimental group, we infused a mixture of 0.1 mM prazosin hydrochloride (prazosin) and 5 mM (S)-(-)-atenolol (atenolol), diluted in ACSF together with a red fluorescent dye (5 mM Alexa 594) for later confirmation of the injection site. For the control group, we injected ACSF together with Alexa 594. Per animal, only one injection was done (either blockers or ACSF) and the animal sacrificed after completion of the recording.

Experimental procedures for in vivo optogenetics

All optogenetic manipulation took place during the first 20 min of each hour between ZT1 and ZT9. A custom-made close-loop detection of NREMS[32] was used for state specificity. In short, NREMS was detected whenever the delta (1 – 4 Hz) to theta (5 – 10 Hz) power ratio derived from the differential frontal-parietal EEG channels crossed a threshold for 2 out of 5 s and the EMG absolute values went below a threshold during at least 3 s. This lead to reliable stimulation during NREMS (Fig. 2), with the exception of a few brief interruptions that occurred during artefacts (e.g. muscle twitches). Optogenetic stimulation of the LC cell bodies was carried out using a PlexBright Optogenetic Stimulation System (Plexon) coupled to a PlexBright Table-top blue LED Module (Wavelength 465 nm) at 1 Hz. Stimulation of

LC terminals in the thalamus or cortex was delivered at 2 Hz (Fig. 3). Optogenetic inhibition of LC cell bodies was performed using a continuous stimulation with a PlexBright Table-top orange LED Module (Wavelength 620 nm) (Fig. 2). Optogenetic stimulation (1 Hz) or inhibition (continuous) was also carried out specifically when sigma power declined or rose, limiting it preferentially to continuity or fragility substates, respectively. This was achieved via a machine-learning-based closed-loop procedure[32] built with a multilayer perceptron model neural network of 10 neurons in the hidden layer and 3 output neurons (for continuity, fragility or none). The network was fed with the last 200 s of a 9th-order polynomial fit of the sigma activity (10 – 15 Hz) calculated for each s. The neural network was then trained, validated, and tested using the sleep scoring from 13 C57BL/6J animals (642,000 epochs) that were otherwise not included in this study. Online, the same data stretches obtained from the mouse in recording were used. For each animal, multiple recording sessions took place with a random allocation of the stimulation protocol: i.e. optogenetic stimulation during NREMS in the LC bodies, its terminals (thalamus for 6 animals or cortex 5 animals), or stimulation of the LC bodies during continuity or fragility substates (in a subgroup of 9 mice). Similarly, for optogenetic inhibition of LC bodies, random allocation of inhibition protocols took place during NREMS (10 animals), continuity or fragility substates (10 animals).

Experimental procedures for in vivo fiber photometry

After the recovery (> 7 d) and habituation to the cabling procedure (> 4 d), we performed two recordings per animal with at least one day between sessions. All recordings were limited to the first 3 – 4 h from ZT1 to minimize possible photobleaching. For fluorescent measurements, we used a pulse-width-modulated sinusoidal signal of 400 Hz using a Raspberry Pi3 (Raspberry Pi Foundation) to modulate a LEDD_2 driver (Doric Lenses Inc.) connected to a blue LED (CLED 465 nm; Doric Lenses Inc.). The power of the driver was set to 200 mA. The blue LED was coupled to a fluorescence MiniCube (iFMC4_IE(400-410)_E(E460-490)_F(500-550)_S, Doric Lenses) that redirected the light to the animal via a low autofluorescence 400-µm-thick fiberoptic patchcord (MFP_400/430/1100-0.57_1m_FMC-ZF1.25_LAF, Doric Lenses Inc.). The cord was connected to the Optic fiberoptic Cannula (MFC_400/430-0.57_3mm_ZF1.25(G)_FLT) implanted in the head of the mouse. A photodetector integrated into the

MiniCube head turned the emitted light from the fluorescent NE sensor into a current signal that was fed into an analog signal of the Intan RHD2132 amplifier board.

In vitro electrophysiological recordings

Thalamic brain slice recordings were performed as previously described in detail[25,59]. Briefly, 3 – 6 weeks after viral injection, DBH-Cre mice aged 8 – 16 weeks were subjected to isoflurane anesthesia, after which they were decapitated, brains extracted and quickly immersed in ice-cold oxygenated sucrose solution (which contained in mM): NaCl 66, KCl 2.5, NaH_2PO_4 1.25, $NaHCO_3$ 26, D-saccharose 105, D-glucose 27, L(+)-ascorbic acid 1.7, $CaCl_2$ 0.5 and $MgCl_2$ 7), using a sliding vibratome (Histocom). Brains were trimmed at the level of the brainstem, glued on the trimmed surface on an ice-cold metal blade and apposed to a supporting agar block on their ventral side. Acute 300-μm-thick coronal brain slices were prepared in the same ice-cold oxygenated sucrose solution and kept for 30 min in a recovery solution at 35 °C (in mM: NaCl 131, KCl 2.5, NaH_2PO_4 1.25, $NaHCO_3$ 26, D-glucose 20, L(+)-ascorbic acid 1.7, $CaCl_2$ 2, $MgCl_2$ 1.2, *myo*-inositol 3, pyruvate 2) before being transferred to room temperature for at least 30 min. All recordings were done at room temperature.

Recording glass pipettes were pulled from borosilicate glass (TW150F-4) (WPI) with a DMZ horizontal puller (Zeitz Instr.) to a final resistance of 2 – 4 MΩ. Pipettes were filled with a K^+-based intracellular solution that contained in mM: KGluconate 140, Hepes 10, KCl 10, EGTA 0.1, phosphocreatine 10, Mg-ATP 4, Na-GTP 0.4, pH 7.3, 290–305 mOsm. Slices were placed in the recording chamber of an upright microscope (Olympus BX50WI) and continuously superfused with oxygenated ACSF containing in mM: NaCl 131, KCl 2.5, NaH_2PO_4 1.25, $NaHCO_3$ 26, D-glucose 20, L(+)-ascorbic acid 1.7, $CaCl_2$ 2 and $MgCl_2$ 1.2. Cells were visualized with differential interference contrast optics and 10X and 40X immersion objectives, and their location within the thalamic ventroposterial medial nucleus or within the somatosensory reticular thalamus could be verified based on previous studies in the lab[25,59]. Infrared images were acquired with an iXon Camera X2481 (Andor). Prior to recording, pipette offset was zeroed, and the stability of the offset verified by monitoring pipette potential in the bath for 10 min. Drifts were < 0.5 mV / 10 min. Signals were amplified using a Multiclamp 700B amplifier, digitized via a Digidata1322A and sampled at 10 kHz with Clampex10.2 (Molecular Devices). Immediately after gaining whole-cell

access, cellular membrane potential and access resistance were measured. Cells included had a resting membrane potential < -55 mV and access resistances < 15 MΩ. The cell types were identified based on their rebound bursting properties (Extended Data Fig. 5). Whole-field blue LED (Cairn Res) stimulation (455 or 470 nm, duration: 0.1 – 1 ms, maximal light intensity 0.16 and 0.75 mW/mm^2 for the two LEDs, respectively). Per slice, only one cell was recorded and exposed to light stimulation. For characterization of LC fiber-evoked membrane depolarizations, cells were held between -65 to -70 mV and exposed to 1 Hz, 3 Hz or 10 Hz stimulation (4 pulses each). Stimulation at different frequencies were applied in random order, with each frequency used maximally twice to avoid run-down of the evoked response. When light-induced depolarizations did not return to the original membrane potential, they were not included in the analysis. For the study of LC-dependent effects on prolonged afterdepolarizations, thalamocortical cells were first injected with series of repetitive negative current injections (100 – 300 pA, 20 pulses, each 120 ms) known to evoke rebound low-threshold Ca^{2+} bursts. Such protocols have been used previously to characterize the cell-intrinsic mechanisms accompanying sleep-spindle-related arrival of barrages of inhibitory synaptic potentials[35]. Following 1 – 2 such repetitive current injections (each followed by 3 – 5 min of recovery time), the current injections were preceded by LC fiber stimulation (10 Hz, 4 pulses) by 5 s, such that the maximum of the LC-evoked membrane depolarization coincided with the end of the negative current injections. For characterization of LC fiber-evoked membrane currents, cells were held in voltage-clamp at -70 mV. Baseline light-evoked currents were evoked maximally 1 – 2 times, followed by bath application of noradrenergic antagonists ((S)-(-)-atenolol (Abcam) for thalamocortical cells or prazosin hydrochloride (Abcam) for thalamic reticular cells) for 5 – 10 min before the next optogenetic stimulation. The in vitro data were manually analyzed using Clampfit v2.2 and as illustrated in Extended Data Fig. 5).

Pharmacological manipulation of heart rate

After the recovery period of the electrode implantation (> 7 d), mice were habituated to the recording conditions for one week. Mice were injected intraperitoneally with NaCl, (S)-(-)-atenolol (1 mg kg^{-1}) (Abcam), a sympathetic antagonist or methylatropine bromide (10 mg kg^{-1}) (Sigma-Aldrich), a parasympathetic antagonist, both known to poorly permeate the blood-brain barrier[60,61]. Injections were

done at 9 am and followed by polysomnographic recording for 100 min. Two recording sessions per drug took place in an intercalated manner. Experimenters were blind to the drug injected.

Histology

After all recording sessions were completed, animals were injected intraperitoneally with a lethal dose of pentobarbital. For animals implanted with electrodes for LFP recording, the position of the electrode was marked via electro-coagulation (50 µA, 8 – 10 s) of the region. Subsequently, ~45 mL of paraformaldehyde (PFA) 4% were perfused intracardially at a rate of ~2.5 mL min^{-1}. Brains were post-fixed for at least 24 h in PFA 4% cooled to 4 °C. Brains were then sliced in 100 µm-thick sections with a vibratome (Microtome Leica VT1000 S; speed: 0.25 – 0.5 mm s^{-1} and knife sectioning frequency: 65 Hz) or a freezing microtome (Microm). Brain sections were directly mounted on slides or kept in well plates filled with 0.1 M PB for later processing. Then, we confirmed the position of LFP electrodes and optic fibers and the fluorescent expression of the injected viruses or local pharmacology injections with a Nikon SMZ25 Stereomicroscope equipped with a Nikon DS-Ri2 16 Mpx color camera. When needed, higher magnification images were acquired using an Axiovision Imager Z1 (Zeiss) microscope equipped with an AxioCam MRc5 camera (objectives used EC-Plan Neofluar 2.5x/0.075 ∞/0.17, 5x/0.16 ∞/0.17, 10x/0.3 ∞/- or 20x/0.5 ∞/0.17).

In vivo data analysis

Scoring of vigilance states: We detected sleep and wake episodes following previous standard procedures in a manner blinded to the treatment[25,32]. For this purpose, we used a custom-made software developed in Matlab (MathWorks) that allows semiautomatic scoring of sleep stages. Shortly, we defined three distinct stages as follows: wakefulness, periods containing large muscle tonus or phasic activity in the EMG signal, together with low-voltage EEG exhibiting fast oscillatory components. NREMS was defined as periods containing low EMG activity together with high amplitude EEG activity showing slow oscillatory components such as slow oscillations (< 1.5 Hz), delta (1.5 – 4 Hz) or sleep spindles (10 – 15 Hz). REM sleep episodes were defined as periods with low EMG activity with prominent Theta (5 – 10 Hz) activity in the EEG. Microarousals were defined as short (< 12 s) periods of wakefulness contained

between the epochs of the same sleep stage. For the intracranial pharmacology experiments, analysis was done for the first 2 h of recording and comparisons were made in a paired manner between the baseline and drug conditions. For all optogenetic experiments, scored data for the first 20 min of each hour (during which light stimulation was done) were compared with the same periods in sham conditions (*ceteris paribus* with the LED turned off). For the fiber photometry experiments, analysis included the complete 3 – 4 h of recordings. For the pharmacological manipulation of the HR, analysis took place for the first 100 min after the i.p. injections.

Analysis of sigma and delta dynamics: Dynamics of sigma (10 – 15 Hz) and delta (1.5 – 4 Hz) activities were quantified from the S1 LFP signal using a wavelet transform with a Mother Gabor-Morlet wavelet with 4 cycles of standard deviation for the Gaussian envelope (see Fig. 1a,c). The frequency dimensions were then collapsed to the two frequency bands of interest, the 10 – 15 Hz sigma band and the 1.5 – 4 Hz delta band. The mean signals were then resampled at 10 Hz and filtered using a 100th order filter with a 0.025 Hz cutoff frequency for further analysis. For NREMS bouts of ≥ 96 s, a Fast Fourier transform was calculated (Fig. 1b) to measure the strength of the 0.02 Hz oscillatory patterns defined here as the area underneath the Fourier transform from 0.01 – 0.04 Hz, subtracting the mean activity between 0.08 to 0.12 Hz (as depicted in Fig. 1b).

Sleep spindle detection, phase coupling analysis and feature extraction: Sleep spindles were detected from the S1 LFP signal for all the experiments. Spindle detection was done using a previously described algorithm[25] that is illustrated in Extended Data Fig. 1. Briefly, we filtered (FIR filter of order 2000) the raw S1 LFP signal in the sigma band (9 – 16 Hz). Then, we squared the signal and applied a threshold of 1.5 the standard deviation above the mean values in NREMS. We then detected all the peaks crossing this threshold and marked as a putative spindle all events containing at least 3 cycles. The starting and ending point of the events were extended to the closest cycle at 0 crossing before and after the threshold, respectively. Events separated by < 50 ms were merged as a single event. For display purposes, we positioned a black dot for each individual spindle event at the center of the spindle in time and a random jittered vertical position.

After spindle detection, we extracted the following features: *Amplitude,* the maximum value of the absolute filtered signal within the event. *Frequency,* mean intra-peak frequency within the detected

spindle event. *Number of cycles* in the spindle. *Duration,* timespan between the beginning and end of the event.

For the analysis of the phase coupling of the spindle events to the sigma activity we first centered the sigma activity at zero by subtracting the mean of the sigma activity in NREMS. Then we constructed a distribution using the phase of the sigma dynamics (calculated as described in *Analysis of sigma and delta dynamics*) at the center of each spindle event (half point between the beginning and the end of the spindle). By using the CircStat toolbox for Matlab (MathWorks)[62], we then confirmed the non-uniformity of the distribution by using the Rayleigh test.

Detection of infraslow cycles: We detected individual cycles of sigma within NREMS using a custom-made Matlab routine. We used the sigma dynamics as described in "*Analysis of sigma and delta dynamics"* and eliminated the regions containing artifacts. Then, we identified the peaks and troughs in the signal with a minimum distance of 25 and 20 s, respectively. Finally, we arranged the positions of successive troughs and kept the starting and ending point for each individual cycle. Next, the marked locations were used to normalize the time in 1000 points for each individual cycle and to interpolate the sigma activity to generate a mean dynamics normalized in time. The same positions were used to normalize the dynamics of NE-related fluorescent signals from the fiber photometry measurements. Only those cycles that within NREMS periods were included in the mean.

Pupil diameter measurements. To standardize the correct location of the optic fibers in the LC cell bodies stimulation or inhibition, we performed pupil diameter measurements in a subset of animals. In short, we set a Basler GigE infrared camera (Basler acA800-510 um, SVGA, 1/3.6'', 510 fps, USB3 Vision) close to one eye of the animal and used a custom-made infrared LED-based lantern directed to the recorded eye to increase the contrast between the pupil and the surrounded area. We built a custom-made software in Matlab (MathWorks) for online or offline pupil detection (using the videos recorded from online trials). First, the user manually selects both the area of interest for the analysis and the initial location of the pupil. Then, for each frame (recorded at 10 fps), a binary image was created using an Otsu's method adaptive threshold with the function `imbinarize` from Matlab (MathWorks). The threshold was set manually to adapt to the conditions of the image and the angles of the infrared light source and the camera. The size of the binary

object closest to the marked pupil was then measured. The dynamics of the pupil diameter was then tracked and z-scored for comparison (See Extended Data Fig. 4).

Fiber Photometry: Changes in bioluminescence were recorded via a photodetector connected to an analog channel in the Intan RHD2000 USB Interface board (Intan Technologies) as described before. The recorded signal fluctuated between 0 – 3.3 V with peaks at 400 Hz as the sinusoidal waveform created to modulate the excitation of the biosensors. The fluorescent dynamics signal was then created using an RMS envelope of 1 s. The changes in biofluorescence $\Delta F * F^{-1}$ were computed by dividing the enveloped signal by its fitted exponential decrease calculated from the dynamics at NREMS.

Cross correlation analysis: To study the similarity of the dynamics between the sigma activity and the NE changes or changes in HR, we performed cross correlation analysis between these two pairs of signals in Matlab (MathWorks). For each long bout (≥ 96 s) of NREMS within the time of analysis (see *Scoring of vigilance states*), we z-scored each signal individually and normalized it to the length of the bout. Then, the cross-correlation was calculated using the function `xcorr` of Matlab and normalized to the length of the bout. Mean cross correlation values were computed for each animal and across animals. Mean correlation coefficient (r) was computed between -5 to 5 s lags.

Heart rate analysis: Changes in HR were computed as previously described[4]. Shortly, EMG signal was filtered using a Chebyshev type 2 high-pass filter. We then differentiated (using the function `diff` from Matlab) and squared the signal to highlight the R peaks. The resulting signal was z-scored to normalize across animals and recording sessions. Then, the R peaks were identified using the Matlab function `findpeaks` with a heuristically found threshold of 0.3 and an interpeak distance of at least 0.08 ms. Peaks with a z-score higher than 10 were considered as artifacts and eliminated. Finally, the HR signal was constructed by measuring the inter-peak time distance and divided by 60 (1 min). An interpolation of the values was performed using the function `interp1` of Matlab and resample at 10 Hz.

Statistics

For the statistical tests, we used R statistical language version 3.6.1. and Matlab (MathWorks). First, we tested for normality of the datasets using the Shapiro-Wilk normality test. For comparisons of two parametric datasets, we used a paired Student's t test and the equivalent Wilcoxon signed rank test for non-parametric

datasets. For comparisons on multiple (> 2) groups of data (as in the case of the amplitude, onset latency and recovery time in the in-vitro experiments), a one-way ANOVA or a Kruskal-Wallis test was used for parametric and non-parametric datasets, respectively. In case of no significance, no further *post-hoc* analysis was performed. In all figures, grey lines denote paired datasets from two conditions (e.g. baseline, opto). Mean values are given by large horizontal lines, error bars indicate standard errors of the mean. Non-parametric *P* values are marked with ^{t}.

Data availability. All data included in this publication will be stored on one of the servers of the University of Lausanne and will be made available once the study is published.

Code availability. Customized MATLAB scripts for data acquisition and analysis are available from the corresponding author upon reasonable request.

Acknowledgements. We thank Paul Steffan and Dr. David McCormick for providing us with the original DBH-Cre breeders. We greatly appreciate the time-efficient support provided to us from Drs. Yulong Li and Jessie Feng regarding the NE sniffers. Particular thanks go to the Animal caretaking team headed by Michelle Blom, and to Titouan Tromme who took so good care of our animal lines. Expert veterinary advice was given by Drs. Delphine Perret and Laure Sériot. We thank Christiane Devenoges for excellent support in histological analysis. We appreciate the helpful exchange regarding optogenetic LC manipulation and NE sniffer experimentation with Drs. Simone Astori, Antoine Adamantidis, Oxana Eschenko, Jessie Feng, Paul Franken, Celia Kjaerby, Maiken Nedergaard, Ernesto Ruben, Andrea Volterra. We are indebted to Francesca Siclari and Christoph Michel for insightful discussions on the human noradrenergic system. Simone Astori and Francesca Siclari provided valuable input on preliminary versions of the manuscript. All lab members provided constructive input to this study throughout the experimental period and to preliminary versions of the manuscript. This study was funded by The Swiss National Science Foundation (n° 310030-184759 to AL), Etat de Vaud and a FBM UNIL PhD Fellowship to AOF.

Author contributions. AOF set up the techniques and acquisition tools for optogenetics, fiber photometry and pupillometry and carried out all in vivo experiments. RC developed the closed loop interference tools, contributed MATLAB scripts, and provided important input to the experiments and analysis. GV carried out in vitro experiments with contributions from AOF and AL. AGG performed many

of the viral injections and helped optimize their reproducibility and GK contributed to the pharmacological studies on HR. LF was involved in methodology and data curation. AL conceived the original experimental plan and developped it further in discussion with AOF, RC and LF and wrote the paper together with AOF. All authors commented on the manuscript and the figures.

Competing interests. The authors declare no competing interests.

Figures and figure Legends

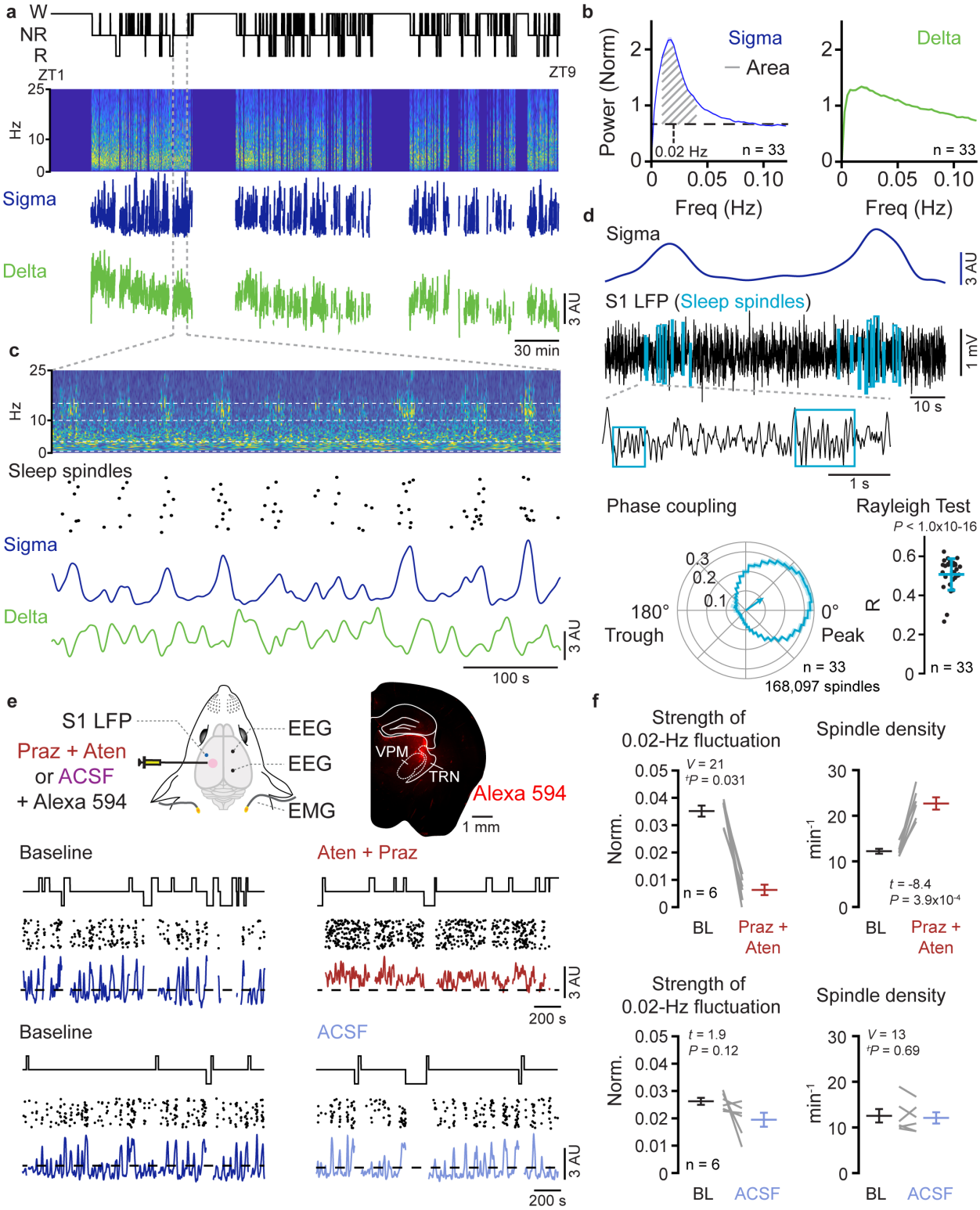

Fig. 1 | The role of noradrenergic signaling for sleep spindle clustering during mouse NREMS. **a**, Hypnogram of a C57BL7/6J mouse from ZT1-ZT9, showing wake (W), NREMS (NR) and REM sleep (R), with corresponding time-frequency distribution of S1 LFP signal below. Power in NREMS only is indicated in color code, with warm colors indicating higher power. Summed sigma (10 – 15 Hz) and delta (1.5 – 4 Hz) power dynamics were derived from the time-frequency distributions. Dashed lines, NREMS bout selected for c. **b**, Fourier transform over sigma (left) and delta (right) power dynamics for n = 33 mice. Diagonal lines, area underneath the Fourier transform used to quantify the strength of the 0.02 Hz-fluctuation in this and subsequent figures 2, 3, 4. Vertical dashed line, 0.02 Hz. Horizontal dashed line, Mean values from 0.08-0.12 Hz. **c**, Single NREMS bout indicated in a. dots, automatically detected spindle events were vertically jittered to visualize single spindles. **d**, Example S1 LFP raw trace taken from c to show detailed position of spindles (see Extended Data Fig. 1). Note how sleep spindles (in blue squares) cluster when sigma power rises (top). 'Phase coupling': sleep spindle occurrence along the 0.02 Hz-fluctuation phases shown in a circular plot; arrow, mean Rayleigh vector across animals. 'Rayleigh test': quantification of the non-uniform distribution via R values ($P < 1.0*10^{-16}$). **e**, Experimental scheme of intracranial local pharmacology in combination with EEG/EMG and S1 LFP electrodes. Prazosin hydrochloride (Praz, 0.1 mM) and (S)-(-)-Atenolol (Aten, 5 mM) or artificial cerebrospinal fluid (ACSF) were co-injected with the red dye Alexa594. Red labeling was verified post-hoc in sections from perfused brains. VPM, ventroposterial medial thalamus, TRN, thalamic reticular nucleus. Traces indicate hypnogram, sleep spindles and sigma power for two mice injected either with Aten + Praz or ACSF. Dashed horizontal line, mean sigma power in Baseline. **f**, Quantification of the strength of the 0.02 Hz-oscillation (as explained in b) and of sleep spindle densities, V, t and *P* values derived from (^{t}) Wilcoxon signed rank or paired t-tests.

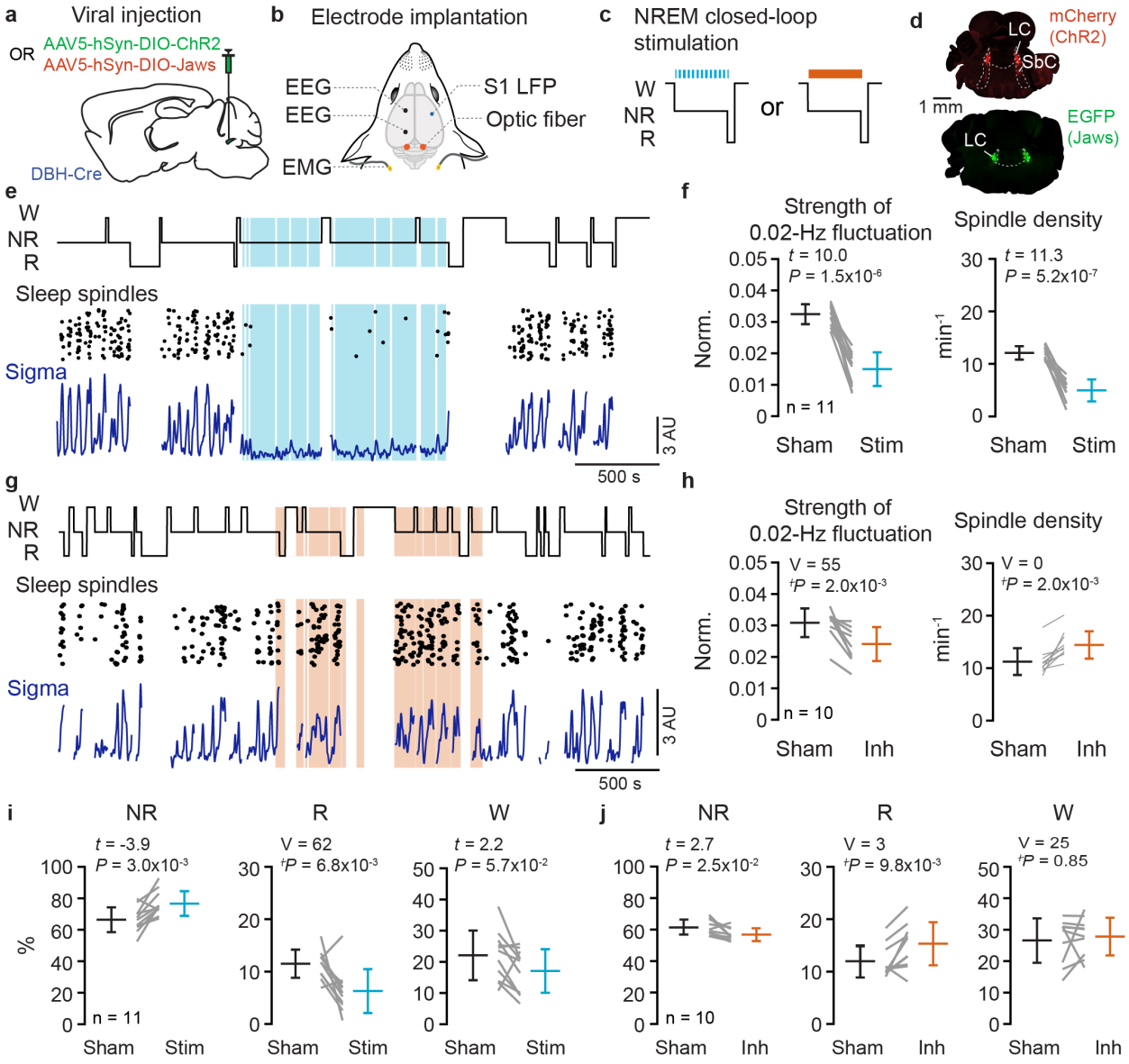

Fig. 2 | Optogenetic interrogation with the locus coeruleus during NREMS. **a**, Viral injection strategy for DBH-Cre mice. For details of the viral plasmids, see Methods. **b**, Experimental scheme for electrode implantation. **c**, Schematic indicating closed-loop stimulation (blue) or inhibition (orange) of LC during NREMS. LC optogenetic interrogation took place in the first 20 min of each hour during 8 h of the light phase (ZT1-9), with light or sham stimulation alternating over successive recording days. **d**, Fluorescent microscopy images confirming viral expression in two mice included in the dataset. **e**, Optogenetic LC stimulation, indicated by blue shading of representative data showing hypnogram, sleep spindles and sigma power derived from S1 LFP recordings. **f**, Quantification of effects on 0.02 Hz-fluctuation strength

and on spindle density. *P* values derived from paired t-tests. **g, h**, Same for optogenetic inhibition. *P* values derived from ([t]) Wilcoxon signed rank test. **i**, Quantification of times spent in NR, R or W during LC stimulation or sham periods. **j**, Quantification of times spent in NR, R or W during LC inhibition or sham periods. V, t and *P* values derived from ([t]) Wilcoxon signed rank or paired t-tests.

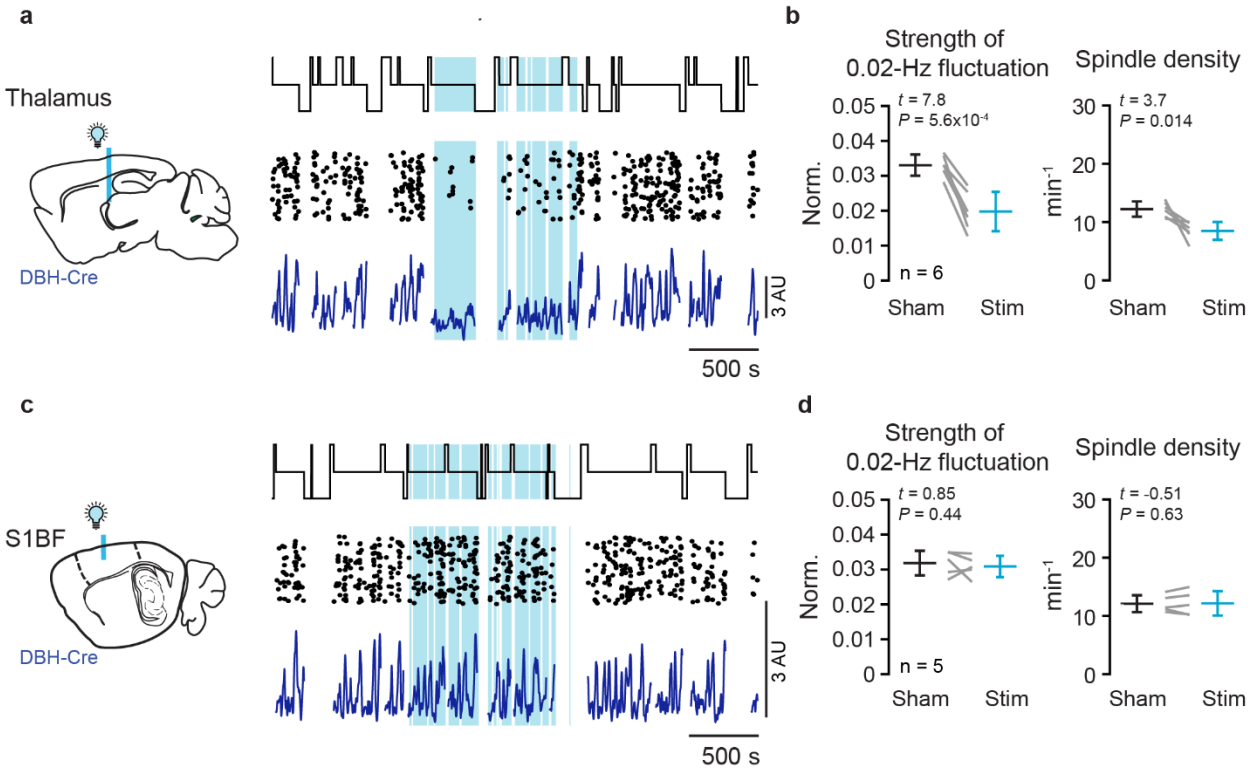

Fig. 3 | Optogenetic interrogation with locus coeruleus afferents in thalamus or cortex during NREMS. **a**, Experimental scheme indicating optic fiber positioning over thalamus. For simplicity, EEG/EMG electrode and S1 LFP electrode are not shown. Representative traces on the right, similar arrangement as in Fig. 2e. **b**, Quantification of effects on 0.02 Hz-fluctuation strength and on spindle density. **c, d**, Same layout for experiments in which the optogenetic fiber was positioned over cortex. All *P* values in the figure derived from paired t-tests.

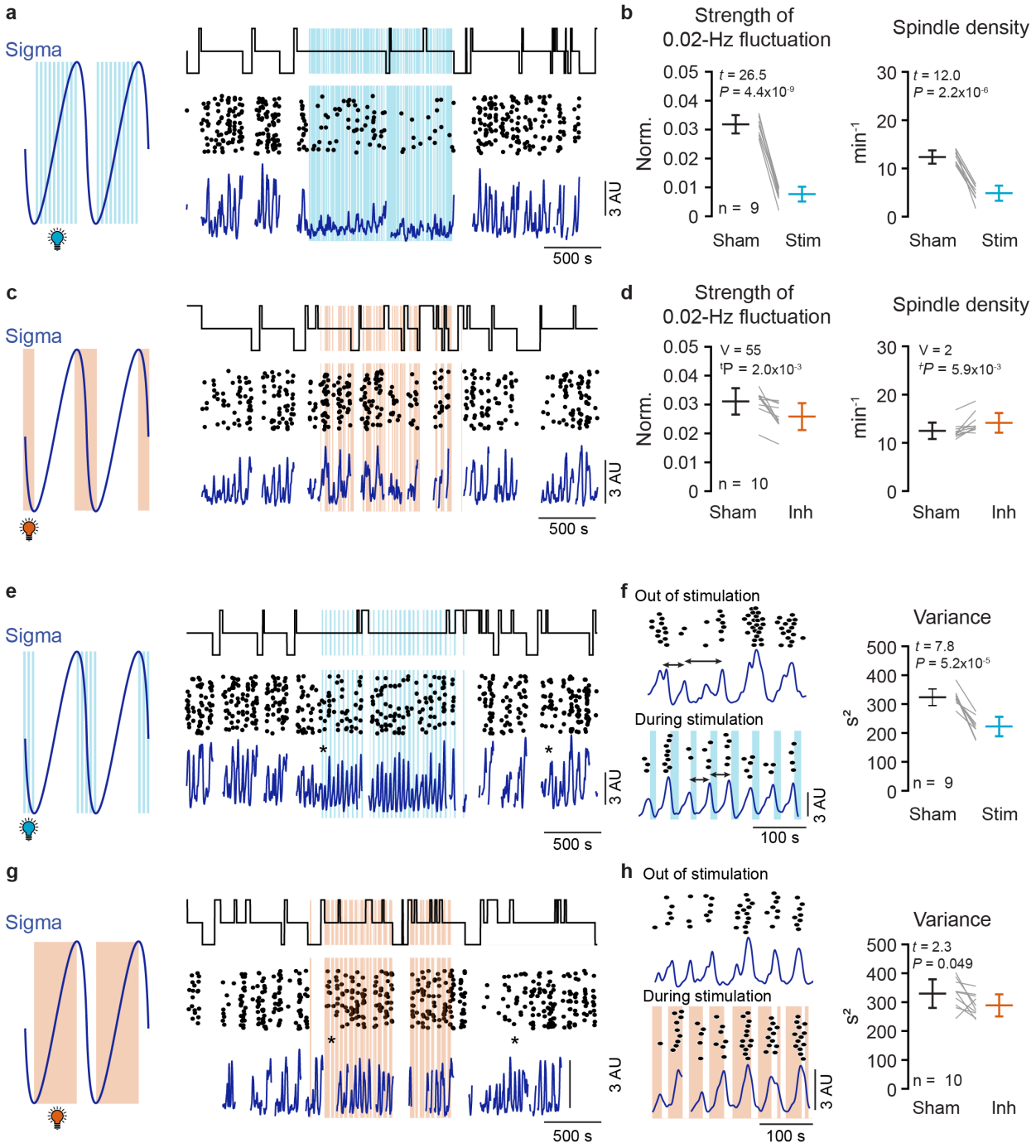

Fig. 4 | Optogenetic interrogation during continuity or fragility substates of NREMS. **a**, LC stimulation during continuity period. Blue waveform, schematic fluctuation to indicate the machine-learning-controlled timing of the light stimuli. Representative traces on the right as in Fig. 2e. **b**, Quantification of effects on 0.02 Hz-fluctuation strength and on spindle density. t and *P* values derived from paired t-tests. **c, d**, LC inhibition during fragility period. Figure panels analogous as in a, b. V, t and *P*

values values derived from (^{t}) Wilcoxon signed rank test. **e,** LC stimulation during fragility periods. Figure panels analogous as in a, c. **f**, Expanded presentation of sigma and sleep spindle traces, taken from moments marked by * in e. Double-headed arrows denote interpeak intervals of the sigma power fluctuation. The regularization of the interpeak intervals in stimulation conditions is quantified through the variance (shown on the right). Note also the tighter temporal alignment between sleep spindles and sigma power. t and *P* values derived from paired t-tests. **g, h**, LC inhibition during continuity period. Figure panels analogous as in e, f. t and *P* values derived from paired t-tests.

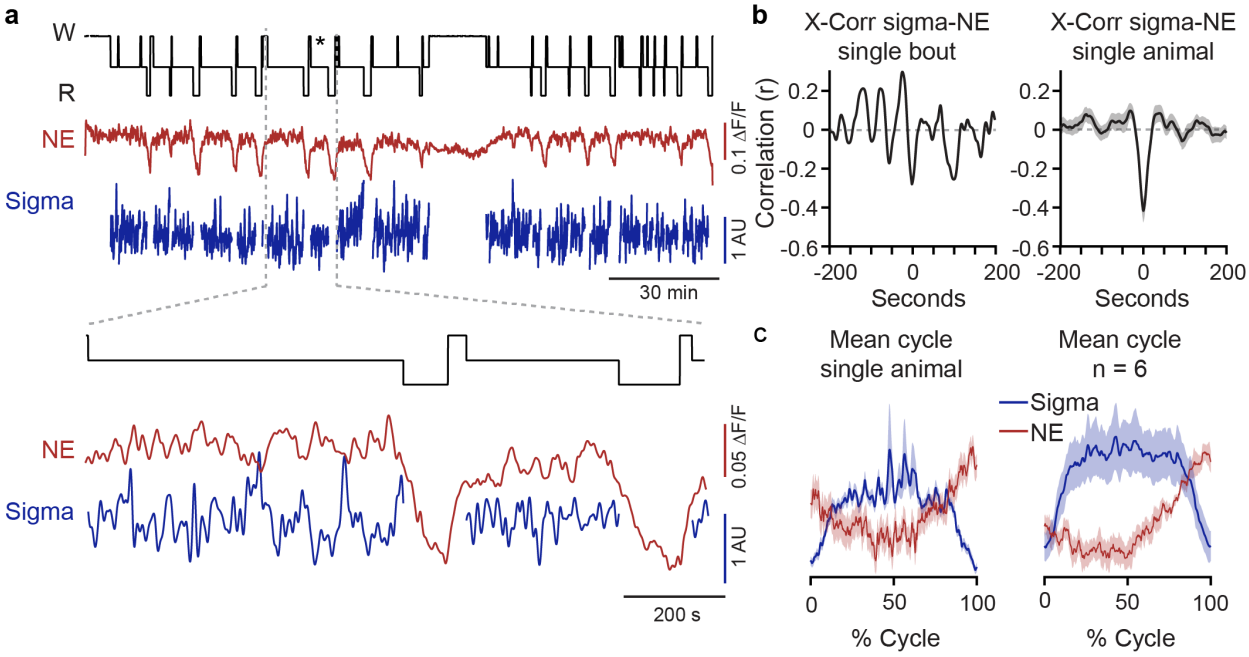

Fig. 5 | Free noradrenaline levels in thalamus anticorrelate with sleep spindles. **a**, Representative recording showing (from top to bottom) hypnogram, relative fluorescence derived from the NE biosensor $GRAB_{NE1ih}$, and sigma power dynamics. Expanded portion shown below. *, bout selected for analysis in b. **b**, Left, Cross-correlation between sigma power and the NE biosensor signal for a single NREMS bout. Right, Mean crosscorrelation across all bouts. **c**, Left, Overlay of sigma power dynamics across all infraslow cycles detected from trough to trough, with corresponding NE fiber photometry signal for one mouse. Right, Mean traces across n = 6 animals.

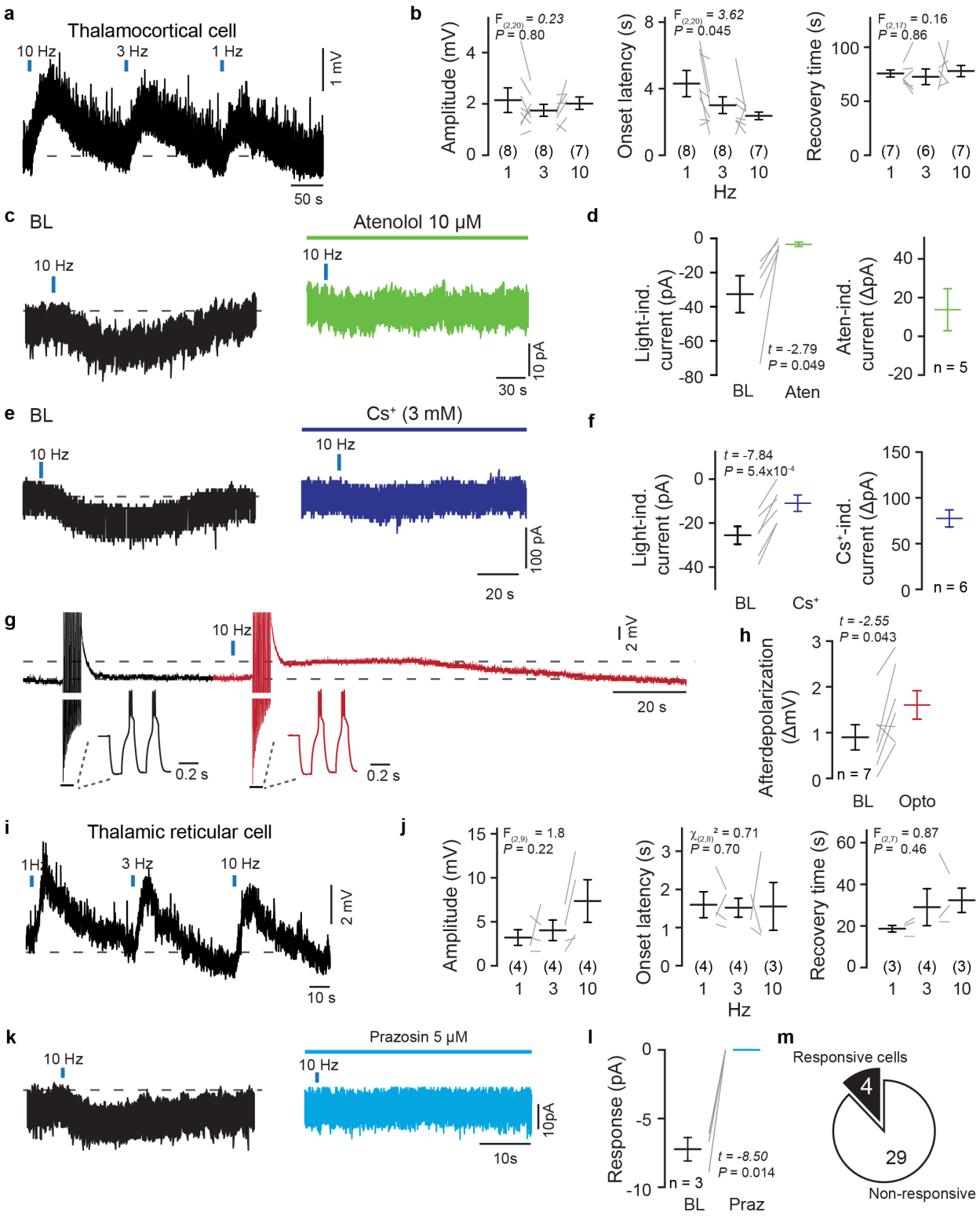

Fig. 6 | LC fiber stimulation evokes slow noradrenergic potentials in thalamic neurons. a, Representative recording from a whole-cell-patched thalamocortical cell exposed to three successive light

stimuli at 10, 3 and 1 Hz (4 pulses, each lasting 100 μs). Dashed line, - 68 mV. **b**, Quantification of evoked response amplitudes, onset latencies and recovery times as explained in Extended Data Fig. 5. F and *P* values from One-way ANOVA followed by post-hoc *t*-tests, which yielded: 1 Hz vs 3 Hz: t = 1.6, *P* = 0.13; 1 Hz vs 10 Hz: t = 2.7, *P* = 0.024; 3 Hz vs 10 Hz: t = 1.1, *P* = 0.29) **c**, Current response in a voltage-clamped thalamocortical neuron held at -70 mV to 10 Hz-light pulses before (left) and after (right) bath application of the β-adrenergic antagonist atenolol. Dashed line, -200 pA. **d**, Left, Quantification of light-induced currents in baseline (BL) and Atenolol (Aten). Right, Aten-induced positive holding current shift. **e,f**, Same as c,d, for bath-application of Cs^+ to block the cAMP-sensitive h-channels. Dashed line, -80 pA. **g**, Example recording from a thalamocortical neuron injected with repetitive negative current pulses (-250 pA, 20 pulses, 120 ms each) to evoke low-threshold Ca^{2+} bursts. Insets show, each, two of these evoked bursts. Burst were followed by an afterdepolarization that was prolonged when light pulses (10 Hz, 4 pulses, blue bar) preceded current injections. Dashed lines, aligned to baseline membrane potential and peak of the afterdepolarization. **h**, Quantification of afterdepolarizations in baseline (BL, without light exposure) and with light exposure (Opto). **i, j**, As a,b, for a representative recording from a thalamic reticular neuron. Dashed line, -72 mV. F and χ^2 derived from ANOVA and Kruskal-Wallis test, respectively. **k,** Current response in a voltage-clamped thalamic reticular neuron held at -70 mV to 10 Hz light pulses before (left) and after (right) bath application of the α1-adrenergic antagonist prazosin. Dashed line, 10 pA. **l**, Quantification of current response amplitude in baseline (BL) and during prazosin (Praz). **m**, Number of TRN cells responding to LC optogenetic fiber stimulation. t and *P* values in d,f,h,l derived from paired t-tests.

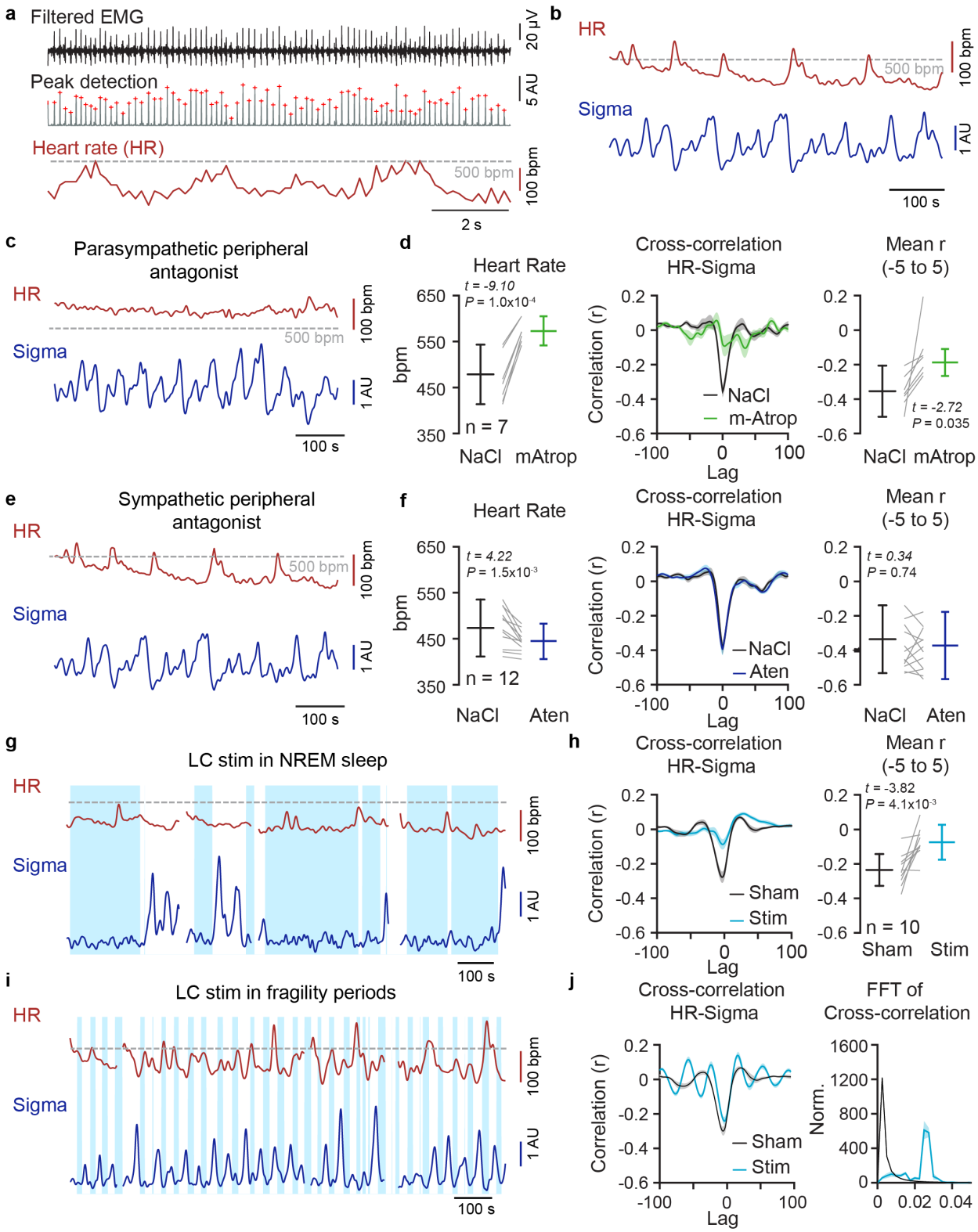

Fig. 7 | The LC as a source of HR variability during NREMS. **a**, Extraction of HR from EMG traces. Top, raw high-pass-filtered (25 Hz) EMG, used for peak detection (middle) and HR (bottom) calculation.

b, Representative NREMS traces showing sigma power dynamics and corresponding HR after an i.p. injection of NaCl. **c**, Example traces illustrating the effects of the parasympathetic antagonist methylatropine (m-Atrop, 10 mg kg^{-1}) on HR and sigma power dynamics. Dashed line, 500 bpm. **d**, Left, Quantification of mean HR following NaCl or m-Atrop injections; Middle, Corresponding Crosscorrelations, Right, Values of the crosscorrelation between -5 to +5 s. **e, f**, As c,d for injection of a sympathetic peripheral antagonist (Atenolol, 1 mg kg^{-1}). **g**, Example traces illustrating the effects of LC stimulation (stim) in NREMS on HR and sigma power dynamics. **h**, Corresponding crosscorrelations quantified as in d, f. **i**, As g, for LC stimulation restricted to machine-learning-detected fragility periods. **j**, Corresponding crosscorrelation and its Fourier transform highlight the appearance of an infraslow peak. All t and *P* values in this figure were obtained from *t*-tests.

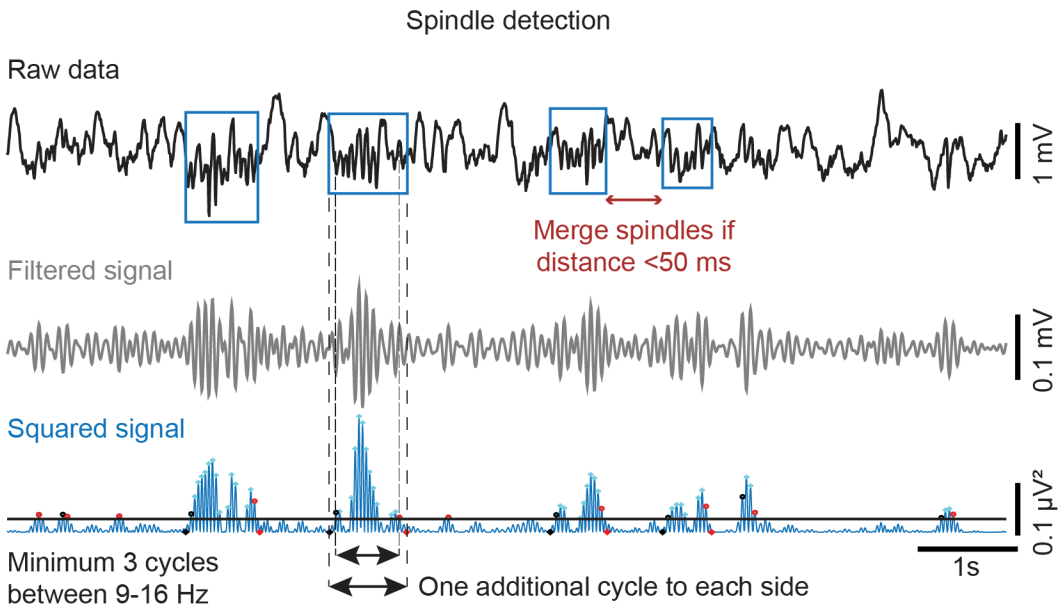

Extended Data Fig. 1 | Method of detection of individual spindles. Raw data from S1 LFP recordings (top), filtered signals (middle) and squared signals (bottom) were used to extract individual spindles according to the criteria given next to the traces. The method was identical to the one published recently[6].

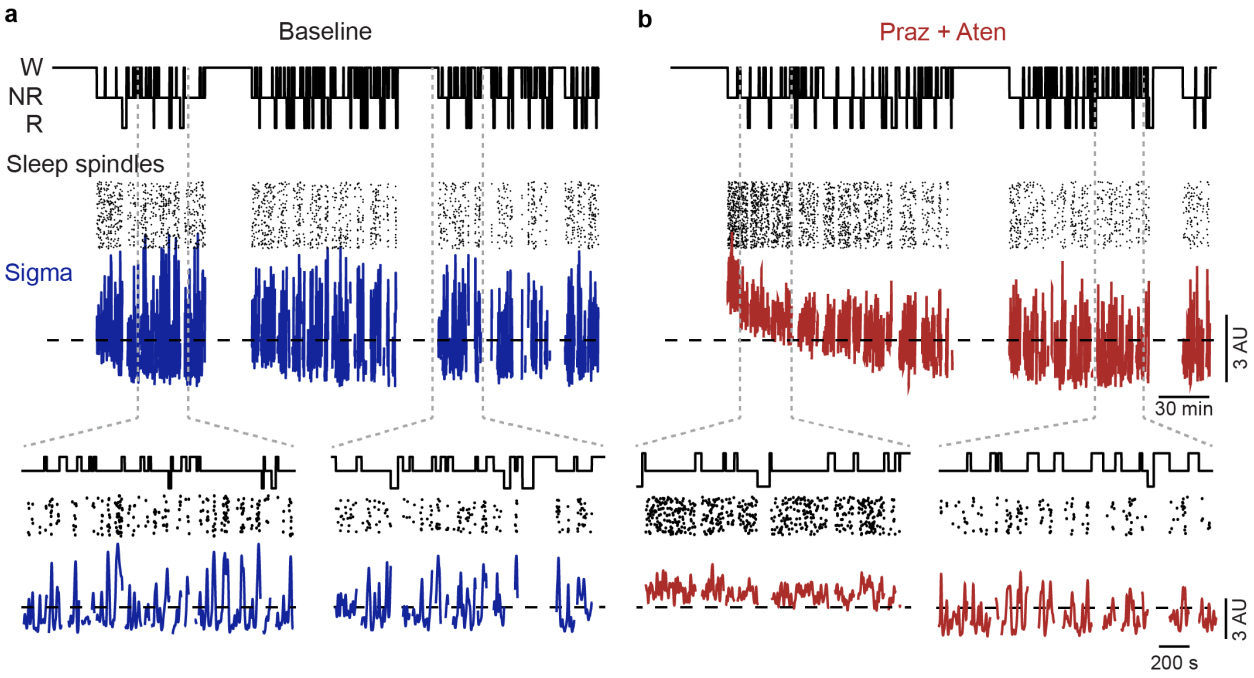

Extended Data Fig. 2 | Time course of pharmacological antagonism of noradrenergic signaling in thalamus on sigma power and sleep spindles. **a**, Animal in baseline conditions, showing, from top to bottom, hypnogram, individual sleep spindles, and sigma power dynamics, with expanded portions shown below. **b**, Same Animal, injected with Praz + Aten. Note slow recovery of the pharmacological suppression of sigma power fluctuations and sleep spindle clustering. Every animal was injected once with either antagonists or ACSF.

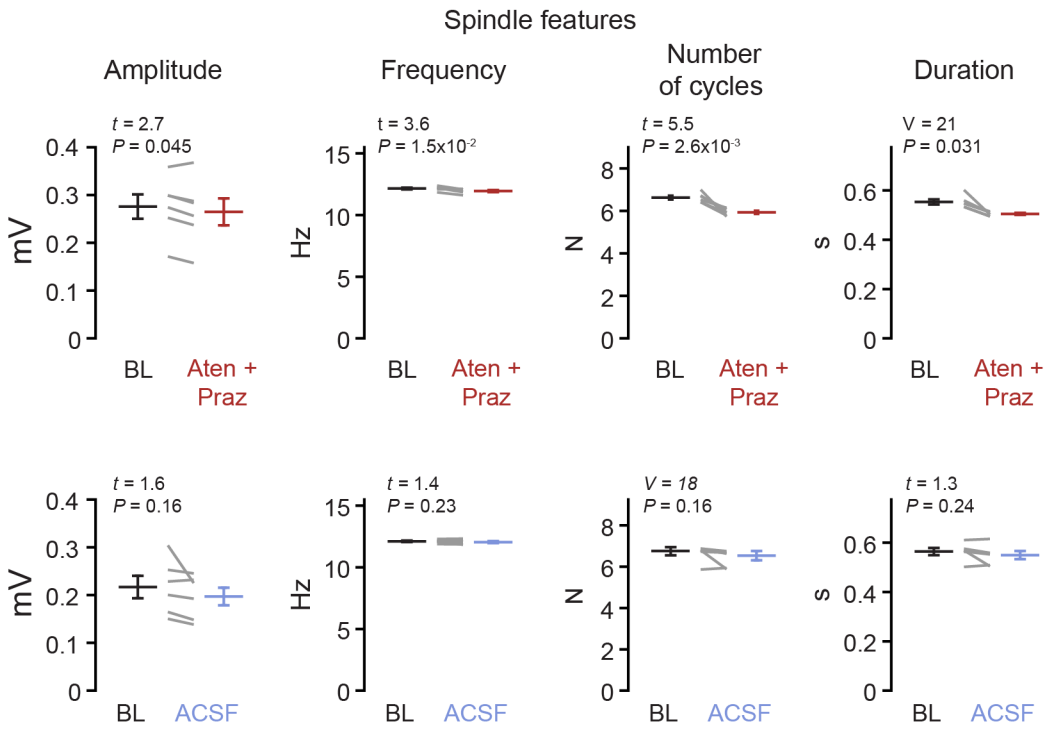

Extended Data Fig. 3 | Quantification of properties of individual sleep spindles in animals used for the pharmacology experiments. Top; Data from the 6 animals injected with antagonists, Bottom; Data from the 6 animals injected with ACSF. From left to right: Peak amplitude, Intra-spindle frequency, Number of spindle cycles, and total spindle duration, analyzed as illustrated in Extended Data Fig. 1 and according to ref. [6]. V, t and *P* in this figure were obtained from ([t]) Wilcoxon signed rank or paired *t*-tests.

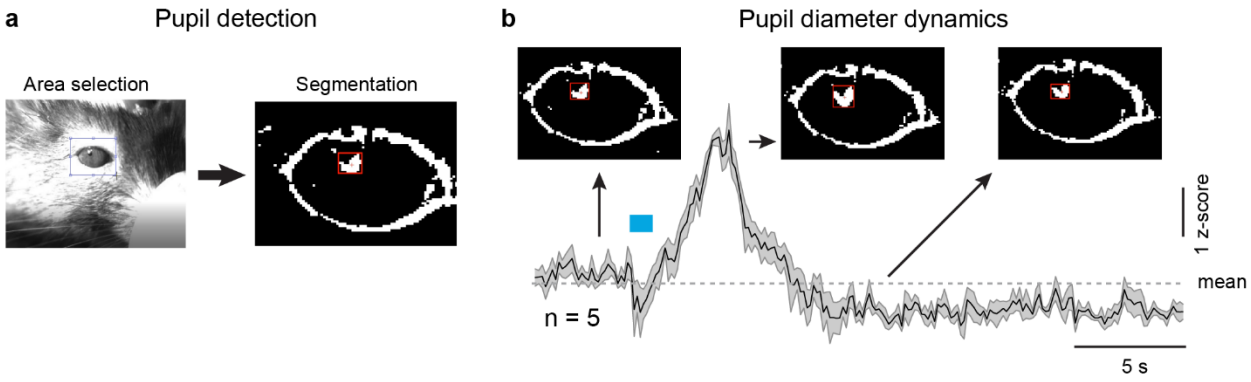

Extended Data Fig. 4 | LC stimulation-induced pupil diameter changes. **a**, Representative image taken from the mouse eye during surgical implantation of optic fiber, showing area selection (dashed square) and corresponding image segmentation with pixels selected for measurement (red square). **b**, Quantification of time course of pupil diameter changes in z-score, with representative segmented images in insets. Blue bar denotes light application. These recordings were made in a subgroup of 5 animals to optimize the position of the optic fiber.

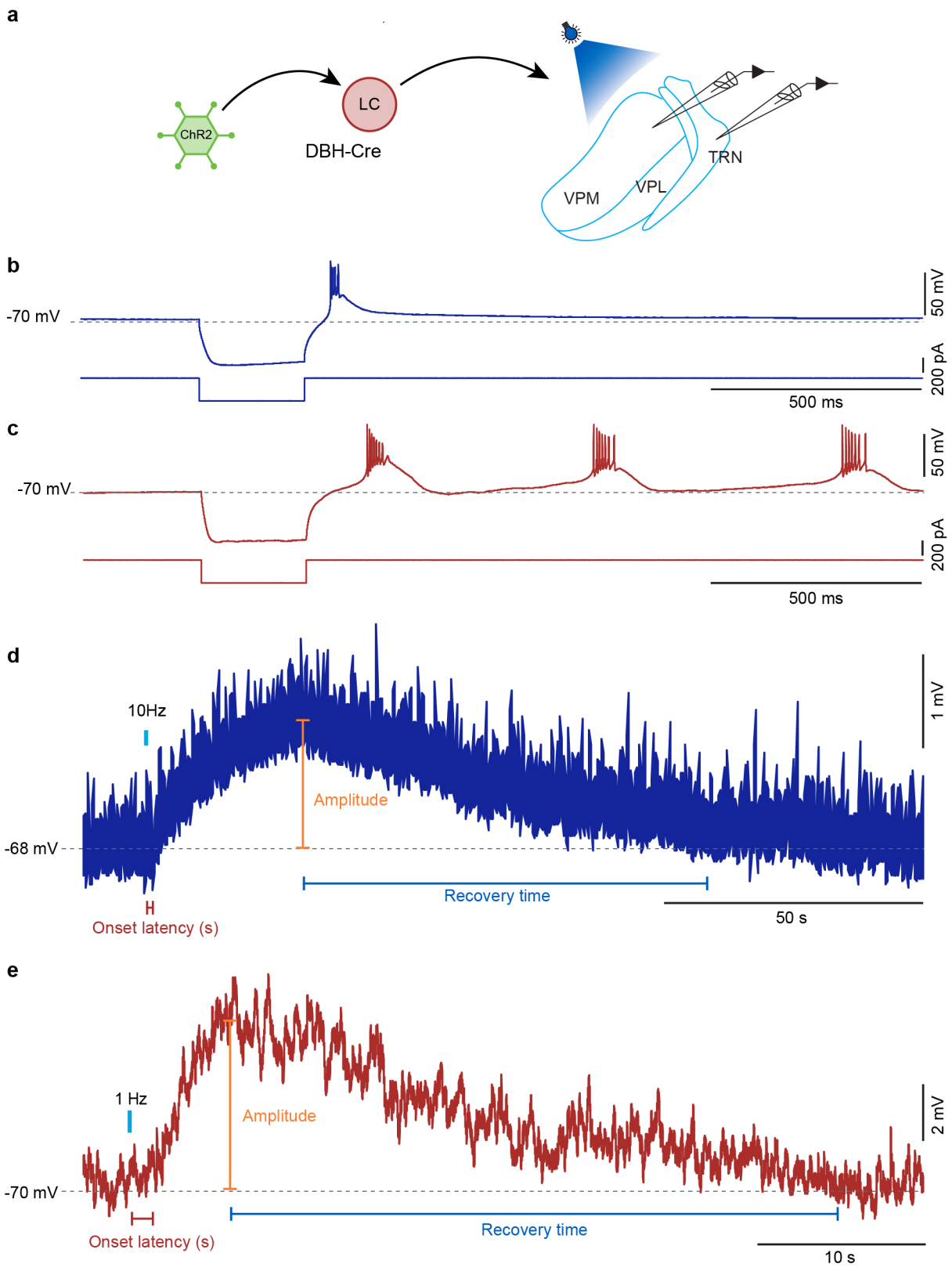
a
ChR2
LC
DBH-Cre
VPM
VPL
TRN
b
-70 mV
50 mV
200 pA
500 ms
c
-70 mV
50 mV
200 pA
500 ms
d
10Hz
Amplitude
-68 mV
Recovery time
Onset latency (s)
1 mV
50 s
e
1 Hz
Amplitude
-70 mV
Onset latency (s)
Recovery time
2 mV
10 s

Extended Data Fig. 5 | Details for the in vitro patch-clamp recordings and analysis. **a**, Schematic showing the experimental design. VPM, ventroposterior medial nucleus, VPL, ventroposterior lateral nucleus, TRN, thalamic reticular nucleus. Recordings were performed in either VPM or TRN while light was shone to activate afferent LC fibers. **b**, Rebound bursting characteristic for a thalamocortical cell recorded in VPM and evoked through brief negative current injection. **c**, Repetitive rebound bursting characteristic for a TRN cell recorded in the somatosensory sector and evoked through brief negative current injection. **d**, Enlarged light-evoked response of a thalamocortical neuron, with indications on how quantification of onset latency, amplitude and recovery time were done. **e**, As d, for a light-evoked response in TRN. Dashed lines denote membrane potential value indicated on the left.